

# Modeling Passive Daytime Radiative Cooling Devices (PDRCs) using COMSOL Multiphysics<sup>TM</sup>

by  
Collins Munene Kariuki

Professor Janice Hudgings, Advisor

A thesis submitted in partial fulfillment  
of the requirements for the  
Degree of Bachelor of Arts  
in Physics

POMONA COLLEGE  
Claremont, California  
May 1, 2024

# Abstract

This thesis delves into the modeling and simulation of Passive Daytime Radiative Cooling (PDRC) devices using COMSOL Multiphysics <sup>TM</sup>, a cutting-edge computational tool. At its core, PDRC technology harnesses the principle of radiative cooling to emit heat directly into outer space, offering a sustainable solution to the pressing challenges of global warming and the energy crisis. By optimizing the optical properties and layering strategies of these devices, the thesis seeks to enhance their cooling efficiency and operational performance, providing a blueprint for future innovations in cooling technologies. By conducting thorough computational analysis and simulations, I validate theoretical models and explore different configurations of basic PDRC designs. My goal is to make a substantial contribution to the development of energy-efficient cooling solutions by examining the reflectance versus wavelength profiles of these designs.

# Acknowledgments

I am deeply grateful to all who have supported me throughout this journey. I extend my heartfelt thanks to Professor Janice Hudgings, whose exceptional guidance, patience, and constant optimism have been a tremendous support, especially during challenging times with COMSOL. Her enthusiasm and faith in the progress of my project have been invaluable.

Special gratitude goes to Professor James Higdon, whose generosity in providing his COMSOL license and desktop was crucial for starting my thesis work. His readiness to help during technical challenges and his provision of essential resources were pivotal to my success.

I also owe a great deal of gratitude to my friends, from suite-mates to peers in the Physics and Computer Science departments, who have consistently offered support and encouragement. The members of the Hudgings lab, too, deserve thanks for their insights and camaraderie.

Lastly, I thank my parents, Anthony Kariuki and Caroline Nyagah. Their nurturing of my curiosity and love for the sciences has shaped me into the inquisitive person I am today. Without their support and sacrifice, I would not be where I am today. Asante na ninawapenda sana!

# Contents

<b>Abstract</b>	<b>i</b>
<b>Acknowledgments</b>	<b>ii</b>
<b>1 Introduction</b>	<b>1</b>
1.1 Cooling is Critical . . . . .	1
1.2 Radiative Cooling . . . . .	2
1.3 Literature Review . . . . .	4
1.3.1 Historical Overview of Radiative Cooling. . . . .	4
1.3.2 Challenges with Material Selection. . . . .	5
1.3.3 Exploration of Polymer Films and Pigmented Paints. . . . .	5
1.3.4 Innovations in Solar Reflectors and Convection Shields. . . . .	6
1.3.5 Photonic Devices and Microstructure Advances. . . . .	6
1.3.6 Future Directions and Microfabrication Techniques. . . . .	7
1.4 Previous Project Work and Project Goals . . . . .	7
<b>2 The Physics Behind PDRCs</b>	<b>9</b>
2.1 Fresnel Equations . . . . .	9
2.1.1 Boundary Conditions for TE Waves . . . . .	11
2.1.2 Boundary Conditions for TM Waves . . . . .	12
2.1.3 Reflection and Transmission Coefficients . . . . .	14
2.1.4 Reflectance and Transmittance . . . . .	16
2.2 Multilayer films . . . . .	20
2.2.1 Transfer Matrix . . . . .	20
2.2.2 Antireflecting Films . . . . .	24
2.2.3 High-Reflectance Layers. . . . .	26
<b>3 Computational Methods</b>	<b>28</b>
3.1 The COMSOL Modelling Workflow . . . . .	28
3.1.1 Setting Up the Model Environment . . . . .	30
3.1.2 Building the Geometry . . . . .	33
3.1.3 Specifying the Material Properties . . . . .	36
3.1.4 Defining the Physics Boundary Conditions . . . . .	39

3.1.5	Build the Mesh . . . . .	41
3.1.6	Run the Study . . . . .	42
3.1.7	Post-Processing the Results . . . . .	43
<b>4</b>	<b>Computational Results</b>	<b>46</b>
4.1	COMSOL: Modeling Anti-Reflectance Coatings . . . . .	47
4.1.1	Anti-reflectance Layers: Setup . . . . .	48
4.1.2	Verifying Anti-Reflectance Computational Results Through Comparison with Theoretical Optics Literature . . . . .	50
4.2	COMSOL: Modeling High Reflectance. . . . .	52
4.2.1	Verifying High Reflectance Computational Results Through Comparison with Theoretical Optics Literature . . . . .	53
4.3	COMSOL: Modeling PDRCs . . . . .	55
4.3.1	Analysis of Silicon Layer Only . . . . .	56
4.3.2	Analysis of Silicon plus Silver Layers . . . . .	59
4.3.3	Analysis of Silicon plus Silver plus PDMS Layers. . . . .	61
<b>5</b>	<b>Conclusion</b>	<b>63</b>
5.1	My work . . . . .	63
5.2	Future Directions . . . . .	63
5.3	Final Remarks . . . . .	64
<b>A</b>	<b>An appendix</b>	<b>65</b>
A.1	About Meshes in COMSOL Multiphysics . . . . .	65
A.2	Additional Resources and Materials Pertaining to This Thesis . . . . .	66

# List of Figures

1.1	Sales of Residential ACs by Country or Region, 2016	2
1.2	Schematic for Radiative Cooling	3
1.3	Ideal Optical Properties of a Radiative Cooling Surface	4
1.4	Experimental Cooling Container by Trombe et al.	5
1.5	Radiative cooling device consisting of seven layers of HfO <sub>2</sub> and SiO <sub>2</sub> , whose thicknesses are defined by extensive numerical optimization (see Methods), on top of 200 nm of Ag, a 20-nm-thick Ti adhesion layer, and a 750-mm-thick, 200-mm-diameter Si wafer substrate. Source: [1]	7
2.1	The transverse electric (TE) set-up	10
2.2	The transverse electric (TM) set-up	13
2.3	Cross sections of the incident, reflected, and transmitted beams	17
2.4	Reflectance vs Angle of Incidence	19
2.5	Multilayer Film Set-Up	21
2.6	Antireflecting Double Layer. Source [2]	24
3.1	The modeling workflow.	29
3.2	The busbar model. Source: [3]	30
3.3	Set-up Screen. Source: [3]	30
3.4	Select space dimension screen. Source: [3]	31
3.5	Select physics screen. Source: [3]	31
3.6	Select study screen. Source: [3]	32
3.7	The COMSOL desktop. Source: [3]	33
3.8	Add geometry button selection. Source: [3]	33
3.9	Application libraries selection. Source: [3]	34
3.10	Application libraries. Source: [3]	35
3.11	COMSOL desktop after adding the busbar geometry. Source: [3]	35
3.12	Explicit choice from the Definitions tab. Source: [3]	36
3.13	Adding bolt selections. Source: [3]	36
3.14	Add Materials option from Materials tab. Source: [3]	36
3.15	Add Materials window. Source: [3]	37
3.16	Assigning some bolts to be made of Titanium. Source: [3]	38
3.17	Material Properties. Source: [3]	38

3.18	The corresponding guiding equation. Source: [3] . . . . .	39
3.19	Electric Currents boundary conditions. Source: [3] . . . . .	40
3.20	Heat Flux boundary conditions. Source: [3] . . . . .	41
3.21	Fine mesh type. Source: [3] . . . . .	42
3.22	Computed results. Source: [3] . . . . .	42
3.23	Application builder button. Source: [3] . . . . .	43
3.24	New Form Wizard button. Source: [3] . . . . .	43
3.25	Form Editor. Source: [3] . . . . .	44
3.26	Test Application results. Source: [3] . . . . .	44
4.1	The double-layer anti-reflectance coating layout (dimensions not to scale). Source: created by the author using Microsoft PowerPoint. . . . .	48
4.2	The triple-layer anti-reflectance coating layout (dimensions not to scale). Source: created by the author using Microsoft PowerPoint. . . . .	48
4.3	COMSOL desktop setup showcasing anti-reflectivity modeling. . . . .	49
4.4	Illustration of the reflectance behavior for two anti-reflective coating config- urations across the visible light spectrum. The blue line indicates the perfor- mance of a quarter-quarter wavelength coating, whereas the green line shows the effect of a quarter-half-quarter wavelength coating. . . . .	49
4.5	Antireflective double-layer arrangement. Source: [2] . . . . .	50
4.6	Anti-reflectance graphs as shown in the optics textbook. . . . .	52
4.7	Anti-reflectance coating with 2 layers, each a $\lambda/4$ thick. . . . .	52
4.8	Anti-reflectance coating with $\lambda/4$ thick bottom layer and $\lambda/2$ thick top layer of $n = 1.6$ . . . . .	52
4.9	Anti-reflectance coating with $\lambda/4$ thick bottom layer and $\lambda/2$ thick top layer of $n = 1.85$ . . . . .	52
4.10	High-reflectance stack comprising double layers with alternating high and low refractive indices. Source: [2] . . . . .	53
4.11	Reflectance spectra for high-low index stacks: (a) for a two-layer double stack, (b) for a six-layer double stack, and (c) for a two-layer double stack enhanced with an additional high-index layer at the very top. Source: [2] . . . . .	54
4.12	Spectral reflectance for a structure with two pairs of high-low refractive index layers, topped with an additional high-index layer. This figure is similar to plot (c) present in the left figure. . . . .	54
4.13	Reflectance comparison for configurations with 5, 11, 21, and 41 layers, each enhanced by an additional high-index surface layer. . . . .	55
4.14	Illustration of a basic PDRC configuration at Hudgings Lab, featuring a silicon base with subsequent layers of silver and PDMS. . . . .	56
4.15	COMSOL desktop setup for PDRC analysis demonstrating the simulation framework. . . . .	56
4.16	Interpolation table for the silicon substrate, showing the wavelength-dependent refractive index. . . . .	57

4.17	Interpolation plot for the silicon substrate, showing the wavelength-dependent refractive index. . . . .	58
4.18	Reflectance variation with wavelength for ( <i>Silicon</i> ) ( <i>Shkondin et al. 2017: n,k 2-20 um</i> ). . . . .	59
4.19	Reflectance variation with wavelength for Silicon, experimentally measured by Fernando Castillo at Hudgings Lab. Measurements were taken at a 10-degree angle from the normal. . . . .	59
4.20	Interpolation table for silver's refractive index. . . . .	60
4.21	Interpolation plot for silver's refractive index. . . . .	60
4.22	Reflectance results for Silicon and Silver Layers . . . . .	61
4.23	Reflectance variation with wavelength for silicon and silver, experimentally measured by Fernando Castillo at Hudgings Lab. Measurements were taken at a 10-degree angle from the normal. . . . .	61
4.24	Reflectance analysis for a composite of silicon, silver, and PDMS. . . . .	62
4.25	Reflectance variation with wavelength for silicon, silver, and PDMS layers, as experimentally determined by Fernando Castillo. The reflectance measurements were conducted at an angle of 10 degrees from the normal. . . . .	62

# Chapter 1

## Introduction

This thesis centers on the modeling of passive daytime radiative cooling devices (PDRCs) utilizing the COMSOL Multiphysics™ software. While all objects with a temperature above absolute zero emit blackbody radiation, PDRCs are distinct in their ability to efficiently radiate heat in the mid-infrared range where the Earth's atmosphere is most transparent. This allows PDRCs to effectively transfer heat directly to the cold sink of outer space during daylight hours, without the need for input energy. Therefore, PDRCs hold the promise of addressing two significant challenges: the energy crisis and global warming.

### 1.1 Cooling is Critical

Over the years, cooling has become more critical to humans due to global warming, rapid population growth and industrial development [4]. Various methods exist for cooling buildings, ranging from traditional practices, such as shading and solar orientation, to the use of electric fans. The most advanced approach is air conditioning (AC), encompassing systems that enhance indoor thermal comfort and air quality. While mechanical cooling techniques date back to the 19th century, widespread adoption of air conditioning began in the 1950s, driven by improved performance, affordability, and economic prosperity, primarily in the United States [5].

Modern AC systems vary widely in size and cost, catering to individual rooms or entire buildings, with electricity being the predominant power source. Today, the largest concentration of cooling systems is found in urban areas, both in industrialized nations and emerging economies, reflecting the higher population density and greater demand for climate control in these regions [5].

Particularly in the realm of residential air conditioners (ACs), China emerges as the foremost market with a staggering sale of 41 million units. Following China, the USA, Japan and the European Union represent the subsequent largest markets for residential ACs. However, there is a significant uptick in sales within various emerging economies, notably in Asia (see Figure 1.1).

Global sales of ACs have exhibited consistent growth in recent years. Over the period

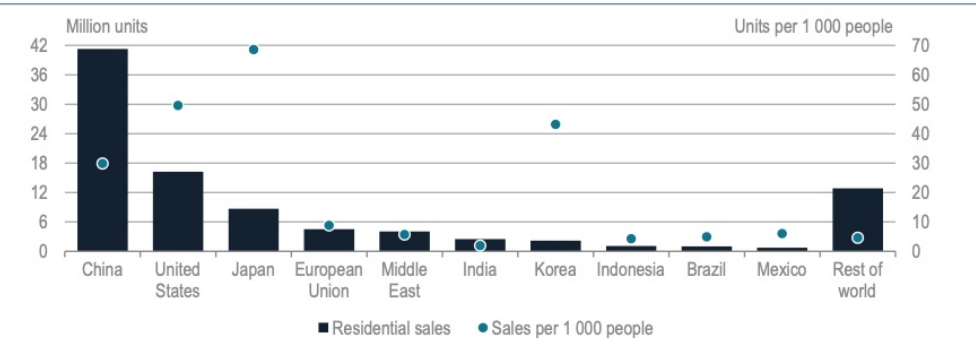
**Figure 1.5 • Sales of residential ACs by country/region, 2016**

Figure 1.1: Sales of Residential ACs by Country or Region, 2016. Source: [5].

from 1990 to 2016, annual AC sales experienced a nearly fourfold increase, reaching 135 million units. In 2016, China emerged as the leading market in terms of AC capacity sales, totaling nearly 390 gigawatts (53 million units) [5].

The growing demand for cooling is significantly influencing power systems, primarily due to the reliance on electricity-driven fans or air conditioners to meet cooling requirements. The escalating demand for air conditioning, in particular, not only elevates overall electricity consumption but also contributes to higher peak electricity loads. Additionally, the emission of greenhouse gases (GHGs) from ACs occurs through refrigerant leakage or improper disposal. It is noteworthy that these refrigerants are potent GHGs with adverse implications for climate change [5].

Improving the efficiency of air conditioning systems (ACs) is pivotal in mitigating peak electricity demand, thereby resulting in decreased emissions and associated financial implications. Endeavors focused on enhancing cooling efficiency necessitate a thorough assessment of the comparative costs linked to diverse cooling technologies.

## 1.2 Radiative Cooling

Objects with temperatures above absolute zero emit blackbody radiation, with a spectrum that depends on their temperature as governed by Planck's law. While the emitted radiation covers a range of wavelengths, it is not uniformly distributed across all wavelengths. Radiative passive cooling occurs when objects emit more radiation, particularly in the infrared spectrum, than the combined radiation they absorb, which includes both blackbody and solar radiation. Thus radiative passive cooling is an electricity-free method for cooling terrestrial entities [6].

The heat emitted by these objects, which exceeds the heat they absorb, is transferred to outer space via thermal radiation, leveraging the substantial temperature difference between Earth (approximately 300 K) and outer space (approximately 3 K) (see Figure 1.2 for net heat loss to space). This process efficiently exchanges heat with the infinite cold reservoir of deep space, achieving cooling without any energy consumption [4].

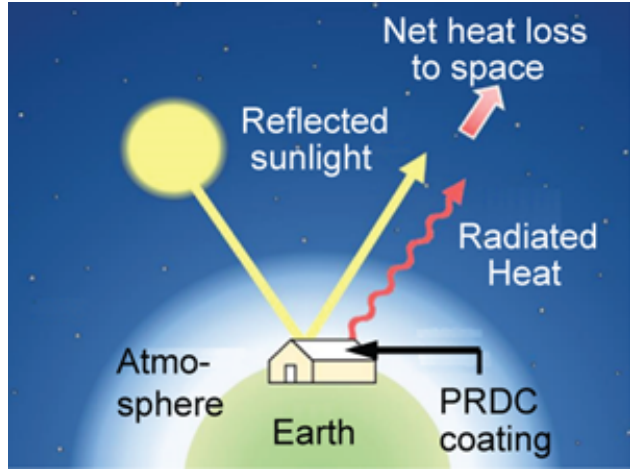


Figure 1.2: Schematic for Radiative Cooling. Source: [6]

Passive radiative cooling can be realized even during the daytime, necessitating precise tuning of optical properties across a broad spectrum of wavelengths, from ultraviolet to mid-infrared (see Figure 1.3). As a result, achieving effective passive daytime radiative cooling imposes stringent requirements on materials and structures to mitigate solar heating [6]:

1. Minimal absorptivity ( $\alpha$ ) approaching 0% (equivalent to nearly 100% reflectance,  $R$ ) in the solar spectrum, ranging from  $0.3\text{--}2.5\ \mu\text{m}$ . This characteristic ensures that the surface absorbs minimal solar energy during daylight, thereby reducing the heat gained by the PRDC.
2. High thermal radiation in the atmospheric transparency window, with an emittance ( $\varepsilon$ ) close to 1 within the long-wavelength infrared (LWIR) transmission window of the atmosphere ( $\lambda = 8\text{--}13\ \mu\text{m}$ ). This range is significant due to the atmosphere's partial transparency and minimal infrared absorption by gas molecules in this spectrum.
3. An emittance ( $\varepsilon$ ) close to 0 in other mid-infrared wavelengths, such as  $5\text{--}8\ \mu\text{m}$  and those greater than  $13\ \mu\text{m}$ . This characteristic is crucial due to the atmosphere's opacity in these spectral ranges, and helps to minimize atmospheric blackbody radiation heating of the device due to its ability to reflect rather than absorb and re-emit infrared radiation in these wavelengths.

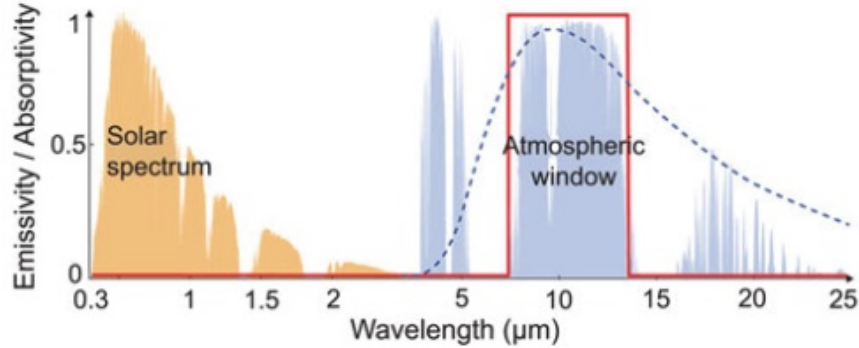


Figure 1.3: Ideal Optical Properties of a Radiative Cooling Surface. It is characterized by a high emissivity,  $\varepsilon = 1$  ( $R = 1$ ), within the long-wavelength infrared (LWIR) atmospheric transparency window. Conversely, within the solar spectrum range, the desired emissivity is minimal,  $\varepsilon = 0$  (or  $R = 0$ ), to avoid radiative heating from the atmosphere. The depicted normalized solar spectrum is shown in orange, while the blue dashed line represents the thermal radiation spectrum for a 300 K blackbody, and the blue shaded area delineates the LWIR atmospheric transparency window. Source: [6]

## 1.3 Literature Review

Passive daytime radiative cooling devices (PDRCs) stand as a sign of optimism amidst the challenges of global warming and the energy crisis. PDRCs are notable not just for their operational efficiency but also for their capacity to transform our approach to energy consumption and environmental conservation. While radiative cooling for nighttime use was established decades ago, only recently has there been significant progress in achieving cooling directly under sunlight, suggesting a promising upward trajectory for the technology's cooling capabilities.

### 1.3.1 Historical Overview of Radiative Cooling.

The concept of radiative cooling, hypothesized by French Engineer Félix Trombe in 1965, initially focused on nighttime cooling. Significant strides have recently been made in achieving daytime cooling under direct sunlight, marking a pivotal advancement in the field. Trombe's collaboration at Montlouis Laboratory led to a cooling method that significantly reduced temperatures of buildings without insulation, leveraging a system that could cool by 14 to 30 degrees Celsius relative to the surroundings [7]. This system involved a north-facing, slightly tilted facade with infrared-transparent panels and a selective radiator, optimizing both night and daytime cooling as seen in Figure 1.4 [8].

Building on Trombe's groundbreaking efforts, in 1975, Catalanotti and his team developed an experimental setup for daytime radiative cooling. This setup combined metals and TEDLAR (polyvinyl-fluoride plastic) to protect the cooling device from direct sunlight, al-

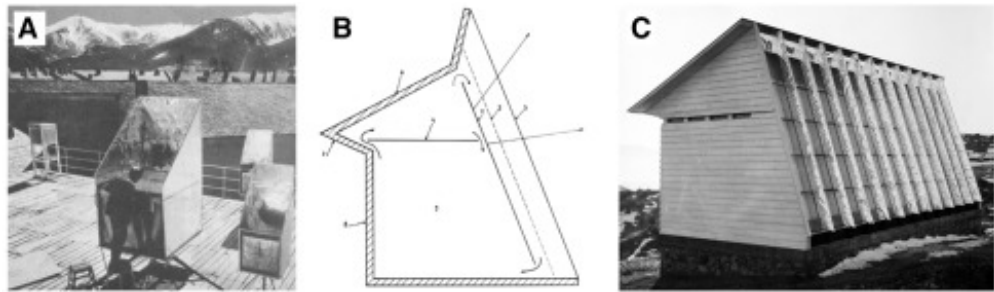


Figure 1.4: Experimental Cooling Container by Trombe and his team in Mont-Louis, France. (A) depicts the experimental cooling setup developed by Trombe's team in Mont-Louis. (B) presents a cross-sectional view of Trombe's patented cold house design. (C) offers a northeast perspective of the cold house, showcasing its radiative cooling facade, a creation of Felix Trombe and his collaborators in 1963. Source: [8]

though it was more effective for nighttime use [9]. This TEDLAR film, offering somewhat selective and high infrared (IR) absorption within the 9 to 13  $\mu m$  wavelength range, also absorbs IR significantly beyond 20  $\mu m$ , impacting its selectivity and, consequently, the efficiency of radiative cooling. Despite this, they achieved a temperature decrease of 10 degrees Celsius below ambient under diffused sunlight. The primary drawback of using PVF polymer for daytime cooling is its substantial absorption in the solar spectrum [10].

Further research explored the potential of thin films on aluminum substrates, with specific material compositions, such as coated thin solid film on an aluminum substrate with  $SiO_6N_{0.2}$  and double layers of  $SiO_2$  and  $SiO_{0.25}N_{1.52}$ , aimed at achieving selective emission [9].

### 1.3.2 Challenges with Material Selection.

Ongoing advancements have aimed to enhance the cooling capabilities of radiative emitters, achieving notable success in nocturnal cooling. Yet, the reliance on both naturally sourced and synthetic polymers has imposed constraints. The absence of materials that combine high solar reflectivity with potent IR emission has hindered effective cooling under direct sunlight. Investigations into selective IR emitters, including polymer films, white pigmented paints, and  $SiO$  films, have encountered limitations due to their inadequate emissivity and the wide range of their IR absorption, which absorbs too much atmospheric radiation, thus failing to significantly lower temperatures below ambient conditions [10].

### 1.3.3 Exploration of Polymer Films and Pigmented Paints.

Additional polymer films such as polyvinylchloride (PVC) and poly(4-methylpentene) (TPX) were evaluated for their potential in radiative cooling. However, their performance, particularly in terms of IR emissivity and selectivity within the crucial 8-13  $\mu m$  range, fell short when compared to PVF [10].

Furthermore, investigations into pigmented paints, inorganic compounds, and gases capable of IR emission for nighttime cooling have shown promise. Specifically, white paint containing titanium dioxide ( $TiO_2$ ), applied to aluminum plates, demonstrated notable cooling effects under clear sky conditions at night, despite less effectiveness under direct midday sun. This suggests pigmented paints might offer advantages for nocturnal cooling due to their application versatility on different substrates [10].

The application of silicon monoxide ( $SiO$ ) films and other inorganic materials in radiative cooling technologies leverages their capacity for targeted infrared (IR) emission. These substances are recognized for their potential to efficiently radiate heat from surfaces, aiding in cooling processes. Nevertheless, their effectiveness is somewhat diminished by a narrow emission bandwidth, limiting the spectrum of IR radiation they can emit. This constraint may decrease the volume of heat dispersed into the environment, thereby affecting the device's cooling efficacy [10].

### **1.3.4 Innovations in Solar Reflectors and Convection Shields.**

Investigations into solar reflectors and IR-transparent materials for daytime cooling have proven effective in both reflecting solar radiation and facilitating IR emission. This capability is essential for daytime cooling to both prevent solar heat accumulation and promote surface heat release. However, maintaining this delicate balance during peak sunlight, when solar irradiance is most intense, presents a considerable challenge. Achieving the optimal mix of solar reflection to avoid overheating while ensuring adequate IR emission for cooling under direct sunlight is particularly complex [10].

Beyond solar reflectors, convection covers or shields significantly enhance a radiative cooler's effectiveness. In daytime operations, when a cooler's net radiative output exceeds its solar absorption, it can significantly lower temperatures beneath the ambient level, assuming convective heat gains are minimized. However, employing convection shields might not always be beneficial, as natural convection can help dissipate heat from the device. Yet, without direct sunlight, convection covers can markedly boost cooling efficiency to its maximum potential [10].

### **1.3.5 Photonic Devices and Microstructure Advances.**

The advancement in photonic-based radiative coolers represents a significant leap towards achieving efficient cooling directly under sunlight, allowing temperatures to fall below ambient levels. This innovative approach differs from traditional methods that rely on the natural optical characteristics of materials, as it harnesses engineered photonic properties in tandem with those natural characteristics to enhance cooling performance [10].

Raman and colleagues conducted the inaugural experiment showcasing radiative cooling under direct sunlight with planar photonic structures (see Figure 1.5), achieving a notable  $4.9^{\circ}C$  drop below ambient temperature. Their device, composed of seven layers alternating between hafnium oxide ( $HfO_2$ ) and silicon dioxide ( $SiO_2$ ) of varied thicknesses, utilized the

upper thick layers for IR emission across the  $8\text{--}13\ \mu\text{m}$  range. The lower, thinner layers on an aluminum-coated silicon wafer reflected up to 97% of solar radiation [1].

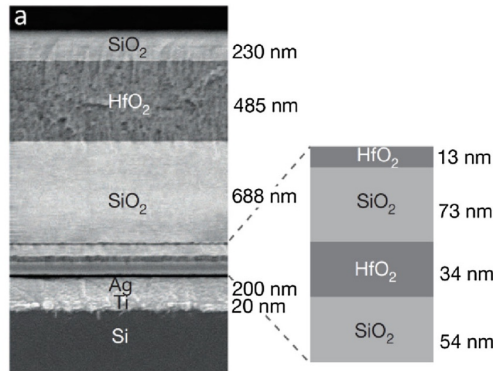


Figure 1.5: Radiative cooling device consisting of seven layers of  $\text{HfO}_2$  and  $\text{SiO}_2$ , whose thicknesses are defined by extensive numerical optimization (see Methods), on top of 200 nm of Ag, a 20-nm-thick Ti adhesion layer, and a 750-mm-thick, 200-mm-diameter Si wafer substrate. Source: [1]

### 1.3.6 Future Directions and Microfabrication Techniques.

Metallic microstructures, like plasmonic structures and metallic photonic crystals, offer the potential for highly selective infrared (IR) emission. Achieving this selective emission across the full  $8\text{--}13\ \mu\text{m}$  wavelength spectrum remains a challenge. Anisotropic metamaterials have shown promise, capable of strong and precise IR emission within this range. This technology could potentially enable cooling significantly below ambient temperatures by more than 10 degrees Celsius, illustrating the advanced capabilities and potential of these engineered materials for effective radiative cooling [10].

Leveraging photonic microstructures for efficient cooling shows great promise but faces hurdles in practical application, particularly for daytime use where such radiators need to be paired with IR transparent solar reflectors to minimize solar absorption. This pairing, however, compromises the precise IR emission. Nonetheless, advancements in microfabrication techniques, like UV-nanoimprint lithography, offer improved prospects for scaling up production, potentially overcoming some of the challenges in deploying these technologies widely [10].

## 1.4 Previous Project Work and Project Goals

In my thesis, I am examining PDRCs composed of a simple three-layer structure: a silicon substrate base, topped with silver to maximize reflectivity, and PDMS to enhance emissivity within the atmospheric window.

Research on PDRCs has been an ongoing project in the Hudgings lab. This thesis aims to build upon the work of Paul McKinley (Class of 2022) and Genevieve DiBari (Class of 2023). McKinley laid the groundwork by developing a rooftop testbed and the fabrication process for PDRCs. DiBari contributed by modeling PDRCs in Python and enhancing the initial outdoor testing setup.

The objective of my research is to develop detailed COMSOL models for the passive daytime radiative cooling (PDRC) devices currently under study in the Hudgings lab. This model aims to quantitatively predict the optical properties, specifically reflectivity  $R(\lambda)$  and emissivity  $\varepsilon(\lambda)$ , across varying wavelengths. By comparing these predictions with empirical data from experimental measurements, the research will evaluate the accuracy of the model and its potential to inform the design and optimization of PDRC structures.

# Chapter 2

## The Physics Behind PDRCs

A passive daytime radiative cooling (PDRC) device operates by absorbing a lower amount of radiation than it emits, thereby facilitating electricity-free cooling, even in daylight conditions. Consequently, one of the pivotal attributes of a PDRC device is the imperative for an absorptivity ( $\alpha$ ) as close to 0% or, conversely, a reflectance ( $R$ ) of 100% within the solar spectrum (ranging from 0.3 to 2.5 micrometers). This specification ensures that the device's surface remains unaffected by solar heating during daylight hours. Additionally, it is critical that the device exhibits an emissivity or absorptivity close to 100% over long wavelengths, particularly within the atmospheric window (ranging from 8 to 13 micrometers), to maximize thermal radiation emission back into space. In this wavelength range, the device's reflectivity should be nearly 0%, which further enhances its cooling efficiency by minimizing the absorption of Earth-emitted radiation, thereby optimizing the device for passive cooling under direct sunlight. See Figure 1.3 for these ideal properties.

To enhance the effectiveness of PDRC, it becomes essential to optimize this reflectivity ( $R$ ) spectrum. One approach for modeling the reflectance spectrum is to treat light as an electromagnetic wave, and from this perspective, ultimately derive  $R$  through the renowned *Fresnel equations*.

The Fresnel equations are mathematical expressions that delineate the proportion of an incident electromagnetic field that is either transmitted or reflected at the interface of two materials with differing refractive indices. This concept aligns precisely with our objectives, as we plan to stack planar materials featuring distinct reflective properties and refractive indices. This chapter serves as an exploration of the theoretical framework underpinning the derivation of  $R$  via the Fresnel Equations, delving into associated phenomena such as total internal reflection. Additionally, we explore the practical application of these principles to PDRC devices.

### 2.1 Fresnel Equations

Consider a light ray incident at point P upon a planar interface between 2 materials, leading to the generation of both reflected and refracted rays. It is important to recognize that the

refractive index before the interface ( $n_1$ ) and after the interface ( $n_2$ ) are properties intrinsic to the materials themselves, determining how light propagates through them. Specifically,  $n_1$  is the refractive index of the material through which the incident and reflected rays travel, while  $n_2$  is the refractive index of the material through which the refracted ray travels. The plane of incidence, lying within the  $x$ - $z$  plane, is defined by both the surface normal and the direction of the incident ray. See Figure 2.1. The derivation below follows from that given in [2].

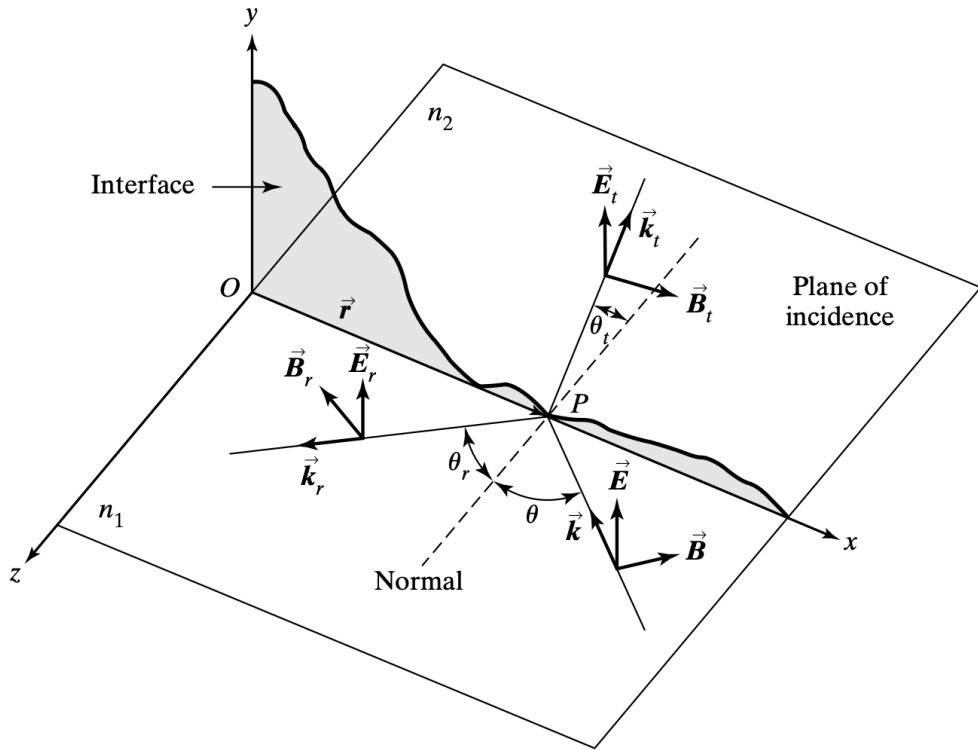


Figure 2.1: This figure illustrates the reflection and refraction of a transverse electric (TE) mode electromagnetic wave at the interface between two media with refractive indices  $n_1$  and  $n_2$ . It shows the incident wave with its electric ( $\vec{E}$ ) and magnetic ( $\vec{B}$ ) fields, the reflected wave with fields ( $\vec{E}_r$ ) and ( $\vec{B}_r$ ), and the transmitted wave with fields ( $\vec{E}_t$ ) and ( $\vec{B}_t$ ), demonstrating the principles of reflection and Law of Refraction for the transmitted wave. The angles of incidence, reflection, and refraction ( $\theta$ ,  $\theta_r$ , and  $\theta_t$ ), and the plane of incidence are also shown. Source: [2]

In the context of each ray, the direction of wave propagation ( $\vec{k}$ ), can be established by the vector cross product of the electric field ( $\vec{E}$ ), and magnetic field ( $\vec{B}$ ) vectors, expressed as  $\vec{E} \times \vec{B}$ . This relationship can be conveniently determined using the right-hand rule, offering a valuable method for directional assessment.

Let us consider that the incident light comprises of plane harmonic waves:

$$\vec{\mathbf{E}} = \vec{\mathbf{E}}_0 e^{i(\vec{\mathbf{k}} \cdot \vec{\mathbf{r}} - \omega t)} \quad (2.1)$$

where  $\vec{\mathbf{E}}$  denotes the electric field vector of the wave at any given point in space, while  $\vec{\mathbf{E}}_0$  represents the amplitude of the electric field, signifying the maximum value that the electric field vector can attain. The wave vector  $\vec{\mathbf{k}}$  provides the direction of wave propagation and its magnitude is the wave number  $k = \frac{2\pi}{\lambda}$ . The position vector  $\vec{\mathbf{r}}$  defines the specific location in space at which the field is evaluated. The angular frequency of the wave is given by  $\omega$ , and the variable  $t$  signifies the time dependence of the wave.  $i$  in the equation shows that the wave possesses both real and imaginary components.

In our analytical approach, we will specifically examine a linearly polarized light wave, where the electric field vector  $\vec{\mathbf{E}}$  is oriented perpendicular to the plane of incidence. According to the right-hand rule, this configuration places the magnetic field vector  $\vec{\mathbf{B}}$  within the plane of incidence. This particular polarization is known as the *transverse electric* (TE) mode

The reflected and transmitted waves can then be expressed as plane harmonic waves:

$$\vec{\mathbf{E}}_r = \vec{\mathbf{E}}_{0r} e^{i(\vec{\mathbf{k}}_r \cdot \vec{\mathbf{r}} - \omega_r t)} \quad (2.2)$$

$$\vec{\mathbf{E}}_t = \vec{\mathbf{E}}_{0t} e^{i(\vec{\mathbf{k}}_t \cdot \vec{\mathbf{r}} - \omega_t t)} \quad (2.3)$$

where  $\vec{\mathbf{E}}_r$  represents the electric field vector of the reflected wave at any point,  $\vec{\mathbf{E}}_t$  represents the electric field vector of the transmitted wave at any point,  $\vec{\mathbf{k}}_r$  is the wave (direction) vector of the reflected wave, and  $\vec{\mathbf{k}}_t$  is the wave (direction) vector of the transmitted wave.

### 2.1.1 Boundary Conditions for TE Waves

At the interface where all three waves occur simultaneously, a crucial boundary condition must be established to govern the relationship between their respective wave amplitudes. This boundary condition stipulates that the waves both incident upon and emerging from the plane of incidence should exhibit continuity and differentiability. This requirement is contingent upon the assumption that the interface is isotropic meaning that the physical properties of the material do not vary with different directions of measurement at the interface.

The boundary conditions derived from Maxwell's equations stipulate that the tangential components of the electric and magnetic fields in plane waves must exhibit continuity across the interface, remaining equal on both sides. It is essential to recognize that while the electric field component is tangential to the interfaces everywhere, the orthogonal nature of the magnetic field vector to the electric field vector necessitates the determination of corresponding tangential magnetic field vectors. When we refer to a field component as being "tangential," we imply that it lies parallel to the plane of the interface, skimming along it without crossing. This is similar to drawing a line that touches a circle at just one point, running along its edge without entering its interior.

In the context of our TE mode configuration (see Figure 2.1), we can express the waves for the incident, reflected, and transmitted electric field components waves as follows:

$$\vec{E} = E\hat{y}e^{i(\vec{k}\cdot\vec{r}-\omega t)} \quad \vec{E}_r = E_r\hat{y}e^{i(\vec{k}_r\cdot\vec{r}-\omega_r t)} \quad \vec{E}_t = E_t\hat{y}e^{i(\vec{k}_t\cdot\vec{r}-\omega_t t)}$$

where  $E$ ,  $E_r$ , and  $E_t$  denote the complex field amplitudes corresponding to the incident, reflected, and transmitted waves, respectively. These waves adhere to the boundary conditions, ensuring the continuity of electric field components parallel to the interface, as in:

$$E + E_r = E_t. \quad (2.4)$$

Using basic trigonometry and Maxwell's equations, we can derive the corresponding magnetic fields for the incident, reflected, and transmitted waves. The expressions for these fields, assuming a TE mode, are:

$$\begin{aligned} \vec{B} &= (B\cos(\theta\hat{x}) - B\sin(\theta\hat{z}))e^{i(\vec{k}\cdot\vec{r}-\omega t)} \\ \vec{B}_r &= (-B_r\cos(\theta_r\hat{x}) - B_r\sin(\theta_r\hat{z}))e^{i(\vec{k}_r\cdot\vec{r}-\omega t)} \\ \vec{B}_t &= (B_t\cos(\theta_t\hat{x}) - B_t\sin(\theta_t\hat{z}))e^{i(\vec{k}_t\cdot\vec{r}-\omega t)} \end{aligned}$$

where  $\theta$  represents the angle of incidence (the angle between the incident wave's direction of propagation and the normal to the interface) (see Figure 2.1),  $\theta_r$  represents the angle of reflection (the angle between the reflected wave's direction of propagation and the normal to the interface), and  $\theta_t$  represents the angle of transmission (the angle between the transmitted wave's direction of propagation and the normal to the interface).

The requirement for continuity in the tangential components of the magnetic field across the interface dictates that the amplitudes of the fields must satisfy the relationship

$$B\cos(\theta) - B_r\cos(\theta) = B_t\cos(\theta_t) \quad (2.5)$$

Here, it's important to note that  $\theta = \theta_r$  according to the Law of Reflection. Equations 2.4 and 2.5 stand as two pivotal equations arising from the boundary conditions for TE waves. These equations, instrumental in determining  $R$ , serve as a critical foundation. Nevertheless, before we delve into the calculation of  $R$  through these boundary conditions, it is imperative to demonstrate the applicability of the same procedure to the transverse magnetic case.

### 2.1.2 Boundary Conditions for TM Waves

Another polarization mode for electromagnetic waves is known as the *transverse magnetic* (TM) polarization. In this mode, the magnetic field vector is oriented perpendicular to the plane of incidence, while the electric field vector lies transverse to the plane of incidence. Within the framework of our TM mode configuration, we can formulate the wave equations governing the electric field components of the incident, reflected, and transmitted waves as follows (see Figure 2.2):

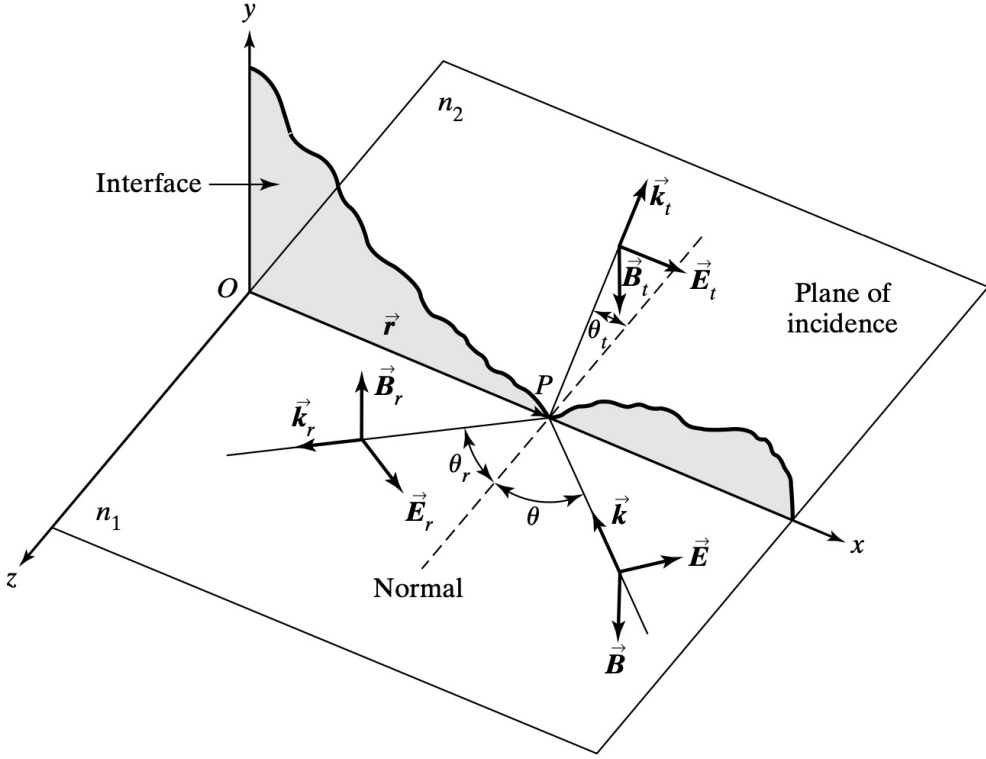


Figure 2.2: This figure illustrates the reflection and refraction of a transverse electric (TM) mode electromagnetic wave at the interface between two media with refractive indices  $n_1$  and  $n_2$ . It shows the incident wave with its electric ( $\vec{E}$ ) and magnetic ( $\vec{B}$ ) fields, the reflected wave with fields ( $\vec{E}_r$ ) and ( $\vec{B}_r$ ), and the transmitted wave with fields ( $\vec{E}_t$ ) and ( $\vec{B}_t$ ), demonstrating the principles of reflection and Law of Refraction for the transmitted wave. The angles of incidence, reflection, and refraction ( $\theta$ ,  $\theta_r$ , and  $\theta_t$ ), and the plane of incidence are also shown. Source: [2]

$$\begin{aligned}\vec{E} &= (E\cos(\theta\hat{x}) - E\sin(\theta\hat{z}))e^{i(\vec{k}\cdot\vec{r}-\omega t)} \\ \vec{E}_r &= (E_r\cos(\theta_r\hat{x}) + E_r\sin(\theta_r\hat{z}))e^{i(\vec{k}_r\cdot\vec{r}-\omega t)} \\ \vec{E}_t &= (E_t\cos(\theta_t\hat{x}) - E_t\sin(\theta_t\hat{z}))e^{i(\vec{k}_t\cdot\vec{r}-\omega t)}\end{aligned}$$

Consequently, the magnetic field components can be written as (see Figure 2.2):

$$\vec{B} = -B\hat{y}e^{i(\vec{k}\cdot\vec{r}-\omega t)}$$

$$\vec{B}_r = B_r\hat{y}e^{i(\vec{k}_r\cdot\vec{r}-\omega t)}$$

$$\vec{B}_t = -B_t\hat{y}e^{i(\vec{k}_t\cdot\vec{r}-\omega t)}$$

These equations adhere to the boundary conditions, guaranteeing the continuity of electric field components parallel to the interface, as demonstrated by:

$$-B + B_r = -B_t \quad (2.6)$$

$$E \cos(\theta) + E_r \cos(\theta) = E_t \cos(\theta_t) \quad (2.7)$$

### 2.1.3 Reflection and Transmission Coefficients

To determine the reflectance  $R$  and, consequently, the transmittance  $T$ , it is imperative to define the reflection ( $r$ ) and transmission coefficients ( $t$ ), as follows:

$$r \equiv \frac{E_r}{E} \quad (2.8)$$

and

$$t \equiv \frac{E_t}{E}. \quad (2.9)$$

However, it is essential to calculate these coefficients for both the Transverse Electric (TE) and Transverse Magnetic (TM) polarization cases. Recall that the electric (E) and magnetic (B) field amplitudes are interconnected through the following relation:

$$E = \nu B = \left(\frac{c}{n}\right) B \quad (2.10)$$

where  $E$  represents the amplitude of the electric field,  $\nu$  represents the phase velocity of the wave within the medium ( $\nu = \frac{c}{n}$ ),  $n$  is the refractive index of the medium, and  $c$  is the speed of light.

We can employ 2.10 to replace every occurrence of  $B$  in the boundary conditions with its corresponding  $E$ . Initiating with the TE case, remember the two vital boundary condition equations for the TE mode:

$$TE : \begin{cases} E + E_r = E_t \\ n_1 E \cos(\theta) - n_1 E_r \cos(\theta) = n_2 E_t \cos(\theta_t) \end{cases} \quad (2.11)$$

We can proceed to solve the system of equations above for the TE case to determine  $r_{TE}$  (by eliminating all instances of  $E_t$ ). Introducing the concept of the *relative refractive index*, denoted as  $n$  and defined as  $n \equiv \frac{n_2}{n_1}$  where  $n_1$  is the refractive index of the initial medium through which the incident wave travels, and  $n_2$  is the refractive index of the second medium into which the wave is transmitted, we can derive:

$$r_{TE} = \frac{E_r}{E} = \frac{\cos(\theta) - n \cos(\theta_t)}{\cos(\theta) + n \cos(\theta_t)}. \quad (2.12)$$

By the Law of Refraction,  $\sin(\theta) = n \sin(\theta_t)$ , so we can eliminate  $\theta_t$  by noting that:

$$n \cos(\theta_t) = n \sqrt{\cos^2(\theta_t)} = n \sqrt{1 - \sin^2(\theta_t)} = \sqrt{n^2 - \sin^2(\theta)} \quad (2.13)$$

Finally, our reflection coefficient is:

$$r_{TE} = \frac{E_r}{E} = \frac{\cos(\theta) - \sqrt{n^2 - \sin^2(\theta)}}{\cos(\theta) + \sqrt{n^2 - \sin^2(\theta)}} \quad (2.14)$$

Likewise, employing our boundary conditions for the TM case along with 2.10, we arrive at the reevaluated boundary conditions for the TM mode, which are as follows:

$$TM : \begin{cases} -n_1 E + n_1 E_r = -n_2 E_t \\ E \cos(\theta) + E_r \cos(\theta) = E_t \cos(\theta_t) \end{cases} \quad (2.15)$$

With this revised form of the boundary condition, we can compute  $r_{TM}$  in a manner similar to our determination of  $r_{TE}$ , resulting in:

$$r_{TM} = \frac{E_r}{E} = \frac{-n^2 \cos(\theta) + \sqrt{n^2 - \sin^2(\theta)}}{n^2 \cos(\theta) + \sqrt{n^2 - \sin^2(\theta)}} \quad (2.16)$$

Similarly, if we follow the same steps we did for evaluating  $r_{TM}$  and  $r_{TE}$ , we can subsequently figure out  $t_{TM}$  and  $t_{TE}$  (we now eliminate  $E_r$  instead of  $E_t$ ). We find:

$$t_{TE} = \frac{E_t}{E} = \frac{2 \cos(\theta)}{\cos(\theta) + \sqrt{n^2 - \sin^2(\theta)}} \quad (2.17)$$

$$t_{TM} = \frac{E_t}{E} = \frac{2 n \cos(\theta)}{n^2 \cos(\theta) + \sqrt{n^2 - \sin^2(\theta)}} \quad (2.18)$$

Observing, for instance, the interconnection between  $t_{TE}$  and  $r_{TE}$ , it is evident that they share the same denominator, suggesting that one can be expressed in terms of the other. To establish the relationship between the two equations, one can subtract  $r_{TE}$  from  $t_{TE}$ , yielding 1. With some additional manipulation, the corresponding equation linking  $t_{TM}$  and  $r_{TM}$  can be derived. Ultimately,  $r$  can be expressed in terms of  $t$  as follows (see Figure 2.2):

$$\begin{aligned} t_{TE} &= 1 + r_{TE} \\ nt_{TM} &= 1 - r_{TM} \end{aligned}$$

The set of equations  $r_{TE}$  (2.14),  $r_{TM}$  (2.16),  $t_{TE}$  (2.17), and  $t_{TM}$  (2.18) constitutes the **Fresnel Equations**. These equations provide reflection and transmission coefficients that establish the connection between incident and reflected electromagnetic field amplitudes in any linear, isotropic, and homogeneous medium. The primary objective of the Fresnel equations is to facilitate the determination of reflectance  $R$  and transmittance  $T$ , which will be discussed in the subsequent subsection.

### 2.1.4 Reflectance and Transmittance

For the sake of energy conservation, it is imperative that, at a specific boundary, the power incident upon the boundary equals the combined power of both the reflected and transmitted waves at that boundary.

$$P_i = P_r + P_t \quad (2.19)$$

We define reflectance  $R$  and transmittance  $T$  as:

$$R = \frac{P_r}{P_i} \quad (2.20)$$

$$T = \frac{P_t}{P_i} \quad (2.21)$$

Hence,  $R$  represents the proportion of reflected power relative to incident power, and transmittance  $T$  signifies the proportion of transmitted power in relation to incident power. This implies that 2.19 conforms to the well-known unity equation, under the assumption of zero absorption:

$$R + T = 1 \quad (2.22)$$

Power can be defined as the product of the irradiance ( $I$ ) of the electromagnetic wave and the cross-sectional area ( $A$ ) through which the wave passes, so 2.19 can be written as:

$$I_i A_i = I_r A_r + I_t A_t \quad (2.23)$$

To ascertain  $A_i$ ,  $A_r$ , and  $A_t$ , it is essential to calculate the cross-sectional area covered by the incident, reflected, and transmitted electromagnetic waves, respectively. By employing trigonometric relationships, as illustrated in Figure 2.3, we can calculate the cross-sectional areas encompassed by the incident, reflected, and transmitted waves and subsequently substitute them into the equation 2.23 to be:

$$I_i A \cos(\theta) = I_r A \cos(\theta) + I_t A \cos(\theta_t) \quad (2.24)$$

where  $A$  represents the cross-sectional area through which the wave propagates.

Using the relation between irradiance and electrical field amplitude,

$$I = E_0^2 \left( \frac{\varepsilon \nu}{2} \right) \quad (2.25)$$

where  $I$  represents the irradiance, which is the power per unit area received by a surface,  $E_0$  is the amplitude of the electric field, indicating the maximum strength of the field,  $\varepsilon$  denotes the permittivity of the medium, and  $\nu$  is the phase velocity of the electromagnetic wave in the medium. Moreover, employing  $\nu_i = \nu_r$  and  $\varepsilon_i = \varepsilon_r$  (since they correspond to the same medium) we can rephrase the power balance equation to be:

$$E_{0i}^2 = E_{0r}^2 + E_{0t}^2 \left( \frac{\nu_t \varepsilon_t}{\nu_i \varepsilon_i} \right) \left( \frac{\cos(\theta_t)}{\cos(\theta)} \right) \quad (2.26)$$

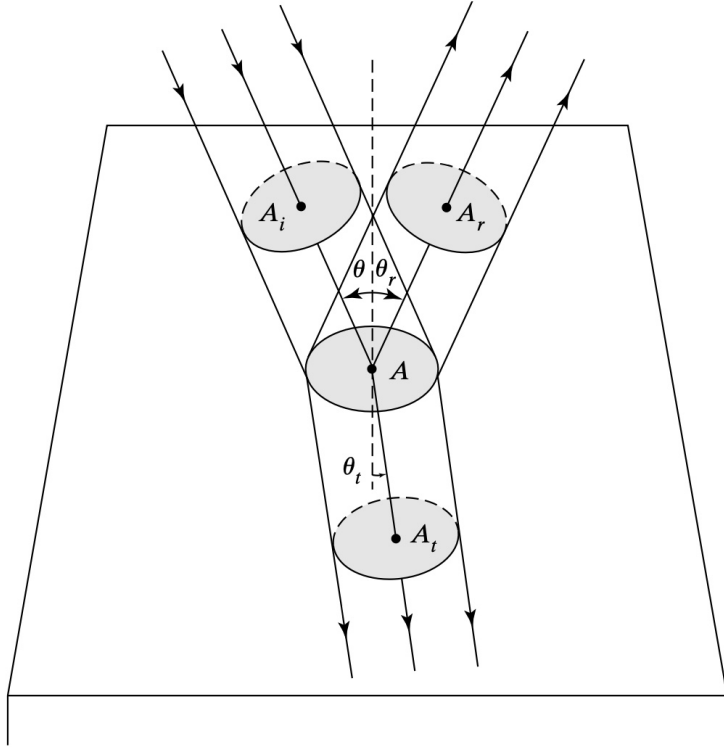


Figure 2.3: Cross sections of the incident, reflected, and transmitted beams. Source: [2]

where  $E_{0i}$ ,  $E_{0r}$ , and  $E_{0t}$  represent the electric field amplitudes of the incident, reflected, and transmitted waves, respectively,  $\nu_i$  and  $\nu_r$  denote the phase velocities in the incident and reflected paths, which are equal since these paths are within the same medium,  $\varepsilon_i$  and  $\varepsilon_r$  are the permittivities of the medium for the incident and reflected waves (equal because they pertain to the same medium), and  $\nu_t$  and  $\varepsilon_t$  refer to the phase velocity and permittivity in the transmission path, respectively.

The ratio  $\frac{\nu_t \varepsilon_t}{\nu_i \varepsilon_i}$  is a complicated way of expressing  $n$ , the relative refractive index. Considering that  $\mu_i = \mu_t = \mu_0$  for nonmagnetic materials, where  $\mu_i$  and  $\mu_t$  are the magnetic permeabilities of the incident and transmitted materials, and  $\mu_0$  is the magnetic permeability of free space, the relationship,  $n^2 = \frac{1}{\mu \varepsilon}$  further elucidates the link between phase velocity, magnetic permeability, and permittivity. Hence, we derive:

$$\frac{\nu_t \varepsilon_t}{\nu_i \varepsilon_i} = \frac{\nu_i^2 \mu_i \nu_t}{\nu_t^2 \mu_t \nu_i} = \frac{\nu_i}{\nu_t} = n \quad (2.27)$$

This transformation streamlines the comprehension of how waves interact with various media by introducing the concept of the relative refractive index,  $n$ . This index represents the ratio of the phase velocities of the wave as it moves from the incident to the transmitted medium, thus quantifying the change in phase speed resulting from the passing of the wave between these two media.

Thus we can include  $n$  in the power balance equations:

$$E_{0i}^2 = E_{0r}^2 + nE_{0t}^2 \left( \frac{\cos(\theta_t)}{\cos(\theta)} \right) \quad (2.28)$$

Dividing through by  $E_{0i}^2$ , we get:

$$1 = r^2 + nt^2 \left( \frac{\cos(\theta_t)}{\cos(\theta)} \right) \quad (2.29)$$

Reflectance ( $R$ ) and transmittance ( $T$ ) quantify the fractions of incident electromagnetic power that are reflected and transmitted across a boundary, respectively. These concepts are grounded in the principle of energy conservation, which, in the context of electromagnetic waves at an interface, is expressed as:

$$R = \frac{P_r}{P_i} = \frac{I_r}{I_i} = \left( \frac{E_{0r}}{E_{0i}} \right)^2 = r^2 \quad (2.30)$$

where in the last step, I have utilized equation 2.25. The term  $r^2$  is introduced as a shorthand notation for this ratio, encapsulating the reflectance in terms of the electric field amplitude ratios.

Looking at equation 2.22, we gather that:

$$T = nt^2 \left( \frac{\cos(\theta_t)}{\cos(\theta)} \right) \quad (2.31)$$

It is worth noting that  $T$  is not merely  $t^2$ , as we must consider the altered speed of the electromagnetic wave when it enters a medium with a different refractive index. This change in speed impacts the rate of energy propagation and, consequently, the power of the beam.

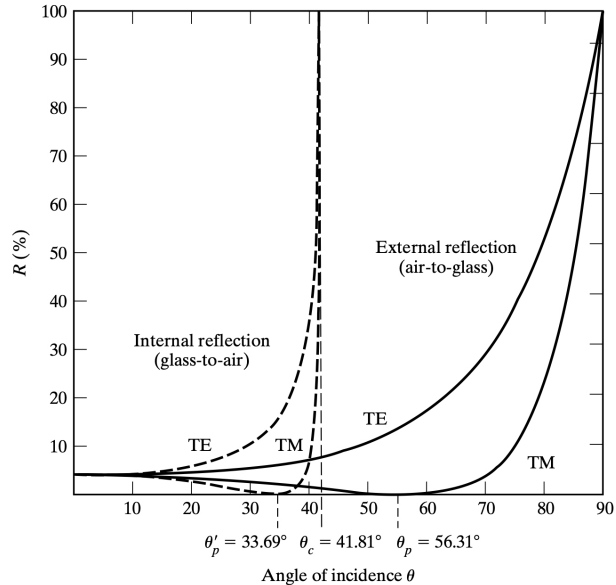


Figure 2.4: This figure shows the reflectance  $R$  (as a percentage) versus the angle of incidence  $\theta$  for TE and TM polarization. The graph differentiates between internal (glass-to-air) and external (air-to-glass) reflections. Importantly, it indicates the critical angle  $\theta_c = 41.81^\circ$  for total internal reflection and Brewster's angles  $\theta'_p = 33.69^\circ$  and  $\theta_p = 56.31^\circ$  for minimal TM reflection. Source: [2]

The theoretical framework outlined by equations 2.30, 2.31, and 2.29 finds a practical illustration in Figure 2.4, which graphs the reflectance  $R$  against the angle of incidence  $\theta$  for both TE and TM polarization. This graphical representation provides a visual confirmation of the relationship between the angle of incidence and polarization effects on reflectance.

The critical angle, denoted as  $\theta_c$ , represents the specific angle of incidence at which a refracted light ray grazes the interface between two media. At this angle, the ray runs parallel to the boundary, without penetrating into the second medium or retreating into the first. When the angle of incidence surpasses  $\theta_c$ , a scenario of total internal reflection unfolds: all the incident light is entirely reflected into the originating denser medium, and no light is refracted into the less dense medium, such as air. This results in the graph indicating a reflectance of 100% for both TE and TM polarization states in situations of glass-to-air transition. This effect is exclusive to internal reflection; conversely, when light travels from a less dense to a denser medium, it is almost always refracted into the denser medium, a behavior consistent across all incidence angles.

Brewster's Angles, marked by vertical dashed lines at  $56.31^\circ$  for external reflection (air-to-glass) and  $33.69^\circ$  for internal reflection (glass-to-air), correspond to the specific angles of incidence where the reflectance reaches a minimum for TM-polarized light in external reflection and internal reflection respectively. At these angles, the reflected intensity is significantly reduced for the respective polarization states.

$n$  is a function of the wavelength ( $\lambda$ ) of light. Consequently, both reflectance ( $R$ ) and

transmittance ( $T$ ) are wavelength-dependent. This wavelength dependence is particularly relevant to the scope of this work as it influences the behavior of light across different spectra. The refractive index's variation with wavelength means that the critical and Brewster's angles, and therefore the efficiency of reflection and transmission, will vary with the wavelength of the incident light, which has significant implications for applications that rely on precise control of light propagation, such as in optical filters and coatings.

## 2.2 Multilayer films

In the development of Passive Daytime Radiative Cooling Devices (PDRCs), we intend to employ multiple stacks comprising diverse materials with distinct refractive indices, arranged in layers to enhance the overall reflection coefficient and consequently increase reflectance. It is crucial to comprehend the electromagnetic wave interaction and optimal layer stacking physics to maximize reflectance. We again need a rigorous consideration of boundary conditions as dictated by Maxwell's equations. The derivation below closely follows that given in [2].

### 2.2.1 Transfer Matrix

At the heart of analyzing how electromagnetic waves interact with thin film structures lies a powerful tool: the transfer matrix. We shall spend most of this section elucidating the process by which we derive a general form of the transfer matrix,  $M$ , for arbitrary thin films. This  $2 \times 2$  matrix is instrumental in establishing a quantitative link between the electric and magnetic fields at one interface. By introducing the transfer matrix, we enable the prediction of wave behavior across various interfaces encountered within a multilayer stack. The transfer matrix not only does this for two layers (single interfaces) but it also offers a scalable approach to tackling the dynamics of multiple layers.

Consider the set-up in Figure 2.5 where the electric field amplitude is perpendicular to the plane of incidence (a transverse electric (TE) wave).

A TE wave propagates from air, reaching the air-film boundary. A fraction of the wave is transmitted, while another portion is reflected. The transmitted portion encounters the film-substrate interface, where part is further transmitted, and another part is reflected. This reflected component then becomes incident on the film-air interface, leading to transmission and reflection, repeating the process. This scenario can be extrapolated to involve multiple films. This complex interplay of transmission and reflection is depicted in Figure 2.5. It is important to note that the film and substrate possess distinct refractive indices, denoted as  $n_1$  and  $n_s$  respectively.

To capture the complex interaction between reflected and transmitted beams, we employ a systematic notation, as seen in the provided setup image. For example,  $E_{r1}$  denotes the aggregate of multiply reflected beams at interface (a), while  $E_{i2}$  signifies the sum of multiple incident beams at interface (b), directed toward the substrate.

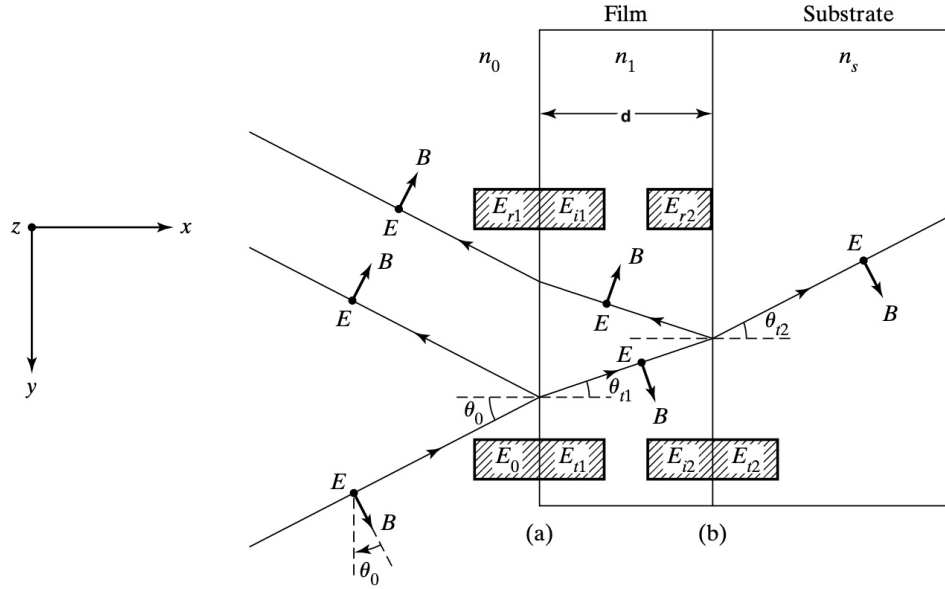


Figure 2.5: Multilayer Film Set-Up. Source: [2]

Continuing with our established assumptions, the film is presumed to be homogeneous, (has the same properties at every point) and isotropic (the physical properties do not differ regardless of the direction or orientation in which it is examined). Furthermore, we hold that the film's thickness is comparable to the wavelength of the incident light because it allows for the film to be a medium where constructive and destructive interference patterns emerge, significantly affecting how light is transmitted and reflected by the film. Such interference phenomena are fundamental in the function of anti-reflective coatings and other optical devices, where precise control of light behavior is required.

This endeavor to identify and equate tangential components of both electric and magnetic fields across an interface lays the foundation for deriving expressions that describe the electromagnetic field behavior across different media. It allows us to formulate relationships that link the characteristics of the fields on one side of the interface to those on the other side, essential for predicting how electromagnetic waves propagate through varying materials.

$$E_a = E_0 + E_{r1} = E_{t1} + E_{i1}, \quad (2.32)$$

$$E_b = E_{i2} + E_{r2} = E_{t2}. \quad (2.33)$$

To determine the tangential magnetic field vectors, trigonometry can be applied to establish the following boundary conditions:

$$B_a = B_0 \cos(\theta_0) - B_{r1} \cos(\theta_0) = B_{t1} \cos(\theta_{t1}) - B_{i1} \cos(\theta_{t1}), \quad (2.34)$$

$$B_b = B_{i2}\cos(\theta_{t1}) - B_{r2}\cos(\theta_{t1}) = B_{t2}\cos(\theta_{t2}). \quad (2.35)$$

We can build on equation 2.10 by expressing B in terms of E as:

$$B = n\sqrt{\varepsilon_0\mu_0}E, \quad (2.36)$$

and since  $c = \frac{1}{\sqrt{\varepsilon_0\mu_0}}$ , we can rewrite 2.34 and 2.35 employing 2.36:

$$B_a = \gamma_0(E_0 - E_{r1}) = \gamma_1(E_{t1} - E_{i1}), \quad (2.37)$$

$$B_b = \gamma_1(E_{i2} - E_{r2}) = \gamma_s E_{t2}, \quad (2.38)$$

where

$$\gamma_0 \equiv n_0\sqrt{\varepsilon_0\mu_0}\cos(\theta_0), \quad (2.39)$$

$$\gamma_1 \equiv n_1\sqrt{\varepsilon_0\mu_0}\cos(\theta_{t1}), \quad (2.40)$$

$$\gamma_s \equiv n_s\sqrt{\varepsilon_0\mu_0}\cos(\theta_{t2}). \quad (2.41)$$

$E_{i2}$  differs from  $E_{t1}$  solely due to a phase difference  $\delta$  arising from a single traversal of the film. The optical path length linked with one traversal is denoted as  $\Delta_1 = n_1 d \cos(\theta_{t1})$ . The optical path length represents the distance that light "perceives" it has covered in a medium and can be quantified in terms of the number of cycles the light beam has undergone within that specific medium. It is inherently proportional to the refractive index and the geometric length of the medium through which light is propagating.

We can express the phase difference that develops due to one traversal of the film as:

$$\delta = k_0\Delta_1 = \left(\frac{2\pi}{\lambda_0}\right) n_1 d \cos(\theta_{t1}). \quad (2.42)$$

Therefore we can express the pair electric field sums  $E_{i2}$  &  $E_{t1}$  and  $E_{i1}$  &  $E_{r2}$  as follows:

$$E_{i2} = E_{t1}e^{-i\delta}$$

$$E_{i1} = E_{r2}e^{-i\delta}$$

and consequently rephrase 2.33 and 2.38 as:

$$E_b = E_{t1}e^{-i\delta} + E_{i1}e^{i\delta} = E_{t2} \quad (2.43)$$

$$B_b = \gamma_1(E_{t1}e^{-i\delta} - E_{i1}e^{i\delta}) = \gamma_s E_{t2} \quad (2.44)$$

Looking at the middle terms, we can solve for  $E_{t1}$  and  $E_{i1}$  in terms of  $E_b$  and  $B_b$ .

$$E_{t1} = \left(\frac{\gamma_1 E_b + B_b}{2\gamma_1}\right) e^{i\delta} \quad (2.45)$$

$$E_{i1} = \left( \frac{\gamma_1 E_b - B_b}{2\gamma_1} \right) e^{-i\delta} \quad (2.46)$$

Utilizing the Euler identities  $2i\sin(\delta) \equiv e^{i\delta} - e^{-i\delta}$  and  $2\cos(\delta) \equiv e^{i\delta} + e^{-i\delta}$ , we can use the equations 2.45 and 2.46 and substitute them into 2.32 and 2.38 to have both:

$$E_a = E_b \cos(\delta) + B_b \left( \frac{i\sin(\delta)}{\gamma_1} \right) \quad (2.47)$$

$$B_a = E_b (i\gamma_1 \sin(\delta)) + B_b \cos(\delta) \quad (2.48)$$

which we can rewrite in matrix notation as:

$$\begin{bmatrix} E_a \\ B_a \end{bmatrix} = \begin{bmatrix} \cos(\delta) & \frac{i\sin(\delta)}{\gamma_1} \\ i\gamma_1 \sin(\delta) & \cos(\delta) \end{bmatrix} \begin{bmatrix} E_b \\ B_b \end{bmatrix}$$

This notation introduces the insightful  $2 \times 2$  matrix that establishes a connection between the electric and magnetic fields at one interface and those at the subsequent interface. Termed the *transfer matrix*, we will refer to this significant matrix in a generic manner as:

$$M = \begin{bmatrix} m_{11} & m_{12} \\ m_{21} & m_{22} \end{bmatrix}$$

Expanding this framework, we can extend the consideration to the stacking of multiple films, leading to the emergence of multiple interfaces. In a more general context, for an arbitrary number  $N$  of layers:

$$\begin{bmatrix} E_a \\ B_a \end{bmatrix} = M_1 M_2 M_3 \dots M_N \begin{bmatrix} E_N \\ B_N \end{bmatrix}$$

with the multiplication of individual transfer matrices representing the entire multilayer stack in the order in which the beam encounters them.

Returning to the comprehensive form of the transfer matrix presented above, we can substitute  $E_a$  and  $B_a$  with the middle segments of equations 2.32 and 2.37. Similarly,  $E_b$  and  $B_b$  can be replaced with the rightmost segments of equations 2.43 and 2.44, resulting in:

$$\begin{bmatrix} E_0 + E_{r1} \\ \gamma_0(E_0 - E_{r1}) \end{bmatrix} = \begin{bmatrix} \cos(\delta) & \frac{i\sin(\delta)}{\gamma_1} \\ i\gamma_1 \sin(\delta) & \cos(\delta) \end{bmatrix} \begin{bmatrix} E_{t2} \\ \gamma_s E_{t2} \end{bmatrix} = \begin{bmatrix} m_{11} & m_{12} \\ m_{21} & m_{22} \end{bmatrix} \begin{bmatrix} E_{t2} \\ \gamma_s E_{t2} \end{bmatrix}$$

Recall  $r \equiv \frac{E_{r1}}{E_0}$  and  $t \equiv \frac{E_{t2}}{E_0}$  (the reflection and transmission coefficients, respectively). By matrix multiplication, we can simplify the resulting equation to obtain:

$$1 + r = m_{11}t + m_{12}\gamma_s t \quad (2.49)$$

$$\gamma_0(1 - r) = m_{21}t + m_{22}\gamma_s t \quad (2.50)$$

Solving for  $r$  by solving the system of linear equations above, we get

$$r = \frac{\gamma_0 m_{11} + \gamma_0 \gamma_s m_{12} - m_{21} - \gamma_s m_{22}}{\gamma_0 m_{11} + \gamma_0 \gamma_s m_{12} + m_{21} + \gamma_s m_{22}} \quad (2.51)$$

## 2.2.2 Antireflecting Films

To gain deeper insights into optimizing reflectance, let us explore the characteristics conducive to anti-reflection using the structure shown in Figure 2.6. Employing a double layer of quarter-wave-thickness films allows for the attainment of minimal reflectance at a specific wavelength. We will examine the simplest scenario for normal incidence, where all angles of incidence, reflection, and refraction are zero.

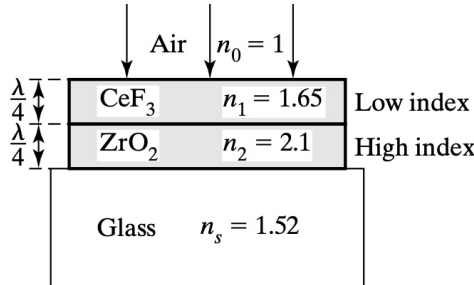


Figure 2.6: Antireflecting Double Layer. Source [2]

At normal incidence ( $\theta = 0$ ) and for a film of quarter-wave thickness where  $d = \frac{\lambda}{4} = \frac{\lambda_0}{4n_1}$ , the phase difference, denoted as  $\delta$ , becomes:

$$\delta = \left( \frac{2\pi}{\lambda_0} \right) n_1 d \cos(\theta_{t1}) = \frac{\pi}{2} \quad (2.52)$$

so that  $\cos(\delta) = 0$  and  $\sin(\delta) = 1$ . With the phase difference established, the corresponding transfer matrix is expressed as:

$$M = \begin{bmatrix} \cos(\delta) & \frac{i \sin(\delta)}{\gamma_1} \\ i \gamma_1 \sin(\delta) & \cos(\delta) \end{bmatrix} = \begin{bmatrix} 0 & \frac{i}{\gamma_1} \\ i \gamma_1 & 0 \end{bmatrix}$$

The term  $\gamma_1$  is related to the refractive index  $n_1$  of the first film layer from the top, Cerium Fluoride ( $\text{CeF}_3$ ), as depicted in Figure 2.6. According to our earlier definitions (equation 2.40),  $\gamma_1 \equiv n_1 \sqrt{\epsilon_0 \mu_0} \cos(\theta_{t1})$  where  $n_1$  is the refractive index of the  $\text{CeF}_3$  layer and  $\theta_{t1}$  is the angle of transmission within this first layer.  $\gamma_1$  is related to the wave impedance within the film relative to the impedance of free space, modified by the cosine of the angle of transmission.

Given two quarter-wave thickness films, the individual transfer matrices are expressed as:

$$M_1 = \begin{bmatrix} 0 & \frac{i}{\gamma_1} \\ i \gamma_1 & 0 \end{bmatrix}$$

and

$$M_2 = \begin{bmatrix} 0 & \frac{i}{\gamma_2} \\ i \gamma_2 & 0 \end{bmatrix}$$

The overall transfer matrix for the system is then the product of  $M_1$  and  $M_2$ :

$$M = M_1 \cdot M_2 = \begin{bmatrix} 0 & \frac{i}{\gamma_1} \\ i\gamma_1 & 0 \end{bmatrix} \begin{bmatrix} 0 & \frac{i}{\gamma_2} \\ i\gamma_2 & 0 \end{bmatrix}$$

Calculating the product of these matrices, we obtain the overall transfer matrix for this double layer:

$$M = \begin{bmatrix} -\frac{\gamma_2}{\gamma_1} & 0 \\ 0 & -\frac{\gamma_1}{\gamma_2} \end{bmatrix}$$

Equation 2.51, the reflection coefficient, then simplifies to:

$$r = \frac{\gamma_2^2 \gamma_0 - \gamma_s \gamma_1^2}{\gamma_2^2 \gamma_0 + \gamma_s \gamma_1^2} \quad (2.53)$$

The reflectance,  $R$ , is simply  $|r|^2$  and using equations 2.39 through 2.41, we can calculate  $R$  to be

$$R = \left( \frac{n_0 n_2^2 - n_s n_1^2}{n_0 n_2^2 + n_s n_1^2} \right)^2 \quad (2.54)$$

Zero reflectance is then expected when the numerator is zero

$$\begin{aligned} n_0 n_2^2 &= n_s n_1^2 \\ \frac{n_2^2}{n_1^2} &= \frac{n_s}{n_0} \end{aligned}$$

so that

$$\frac{n_2}{n_1} = \sqrt{\frac{n_s}{n_0}} \quad (2.55)$$

For a glass substrate with a refractive index of  $n_s = 1.52$  and incidence from air with  $n_0 = 1$ , the optimal ratio of the refractive indices for the two films should be  $\frac{n_2}{n_1} = \sqrt{1.52} \approx 1.23$ . However, achieving near-zero reflectance is challenging over the broader region of the visible spectrum because the refractive index of each material in the layers vary with wavelength.

In the visible spectrum, which ranges approximately from 400 to 700 nm, each wavelength interacts differently with the optical materials based on their refractive index at that specific wavelength. The optimal thickness and refractive index that reduce reflectance for one wavelength will not necessarily be optimal for another due to this dispersion. Furthermore, the phase change upon reflection at the boundary of a medium also varies with wavelength, which affects the constructive and destructive interference patterns needed for anti-reflective properties.

Practically, this requires a careful design of the coating's material properties and thicknesses to achieve broader-wavelength anti-reflection. This design must account for the wavelength-dependent change in refractive indices and the cumulative effect of multiple reflections and transmissions at different interfaces within the multilayer stack, which becomes

increasingly complex as the wavelength range widens, hence the difficulty of zero reflectance across the broader region over the visible spectrum.

This dependence of refractive index on  $\lambda$  introduces a level of complexity that is difficult to treat analytically, underscoring the necessity for using COMSOL. By leveraging COMSOL's robust simulation capabilities, the overall goal is to accurately model  $R(\lambda)$  for PDRCs over a wide visible-IR spectrum, enabling detailed analysis and optimization.

### 2.2.3 High-Reflectance Layers.

In the previous section, we established that to optimize for anti-reflectance, we stack layers in the order of air-low index-high index-substrate. Conversely, to optimize for high-reflectance, we follow the opposite order: air-high index-low index-substrate. A set of double layers designed to enhance reflectance is referred to as a *high-reflectance stack* or *dielectric mirror*.

The transfer matrix for the two films in the order of high index-low index is

$$M_{HL} = \begin{bmatrix} 0 & \frac{i}{\gamma_H} \\ i\gamma_H & 0 \end{bmatrix} \begin{bmatrix} 0 & \frac{i}{\gamma_L} \\ i\gamma_L & 0 \end{bmatrix} = \begin{bmatrix} -\frac{\gamma_L}{\gamma_H} & 0 \\ 0 & -\frac{\gamma_H}{\gamma_L} \end{bmatrix}$$

For  $N$  similar double layers, we obtain  $M = (M_{HL})^N$ . In matrix form,

$$M = \begin{bmatrix} 0 & \frac{i}{\gamma_L} \\ i\gamma_L & 0 \end{bmatrix}^N = \begin{bmatrix} \left(-\frac{\gamma_L}{\gamma_H}\right)^N & 0 \\ 0 & \left(-\frac{\gamma_H}{\gamma_L}\right)^N \end{bmatrix}$$

Considering normal incidence and using equations 2.39 through 2.41,

$$\frac{\gamma_L}{\gamma_H} = \frac{n_L}{n_H}. \quad (2.56)$$

Equation 2.51, the reflection coefficient, then simplifies to:

$$r = \frac{n_0 \left(\frac{-n_L}{n_H}\right)^N - n_s \left(\frac{-n_H}{n_L}\right)^N}{n_0 \left(\frac{-n_L}{n_H}\right)^N + n_s \left(\frac{-n_H}{n_L}\right)^N} \quad (2.57)$$

To get  $R$ , we calculate  $|r|^2$  to get

$$R = \left[ \frac{\left(\frac{n_0}{n_s}\right) \left(\frac{n_L}{n_H}\right)^{2N} - 1}{\left(\frac{n_0}{n_s}\right) \left(\frac{n_L}{n_H}\right)^{2N} + 1} \right]^2 \quad (2.58)$$

Maximum (100%) reflectance is either achieved when:

1.  $N$  (the number of layer pairs) approaches infinity.

2.  $\frac{n_L}{n_H}$  approaches zero. For example, when this ratio is 0.5 and there are 3 layers, a reflectance of 95.97 is achieved.

Since the optimal reflectance is obtained with the smallest ratio of  $\frac{n_L}{n_H}$ , high-reflectance stacks can be constructed using alternating layers of  $MgF_2$  ( $n_L = 1.38$ ) and  $ZnS$  ( $n_H = 2.35$ ) or  $TiO_2$  ( $n_H = 2.40$ ). For example, employing alternating double layers of  $MgF_2$  and  $ZnS$  can achieve a reflectance of 99.95% with a layer count ( $N$ ) of 8.

In this chapter, we have meticulously explored the theoretical underpinnings of PDRCs, delving into the Fresnel Equations, the boundary conditions for TE and TM polarization states, and the complex behavior of multilayer films. Our investigation highlighted the delicate balance between film thickness, the coherence of light, and the manipulation of refractive indices necessary to realize passive cooling without external energy. Moreover, the transfer matrix is a formidable mathematical apparatus, enabling us to analyze the traversal of light through successive film layers. The knowledge acquired is instrumental for advancing PDRC technologies that promise to redefine sustainable energy practices. These strategies leverage essential physical laws to confront the current urgent environmental and energy demands.

# Chapter 3

## Computational Methods

COMSOL Multiphysics™ is a comprehensive software suite for finite element analysis, solving, and simulation across a wide array of physics and engineering disciplines, particularly focusing on coupled phenomena and multi-physics interactions. It enables the creation and simulation of physics-based models and applications in an intuitive, interactive workspace.

COMSOL software supports a broad spectrum of applications, from electromagnetics and structural mechanics to acoustics, fluid dynamics, heat transfer, and chemical engineering. COMSOL features an extensive array of modules, including the Wave Optics module for optical applications simulations like wave propagation in fiber optics and photonics, the Semiconductor module for the analysis of semiconductor devices such as diodes and transistors, and the AC/DC module for examining electric and magnetic fields in static and low-frequency scenarios.

For my thesis, which involves analyzing ray paths in optical systems, I will be utilizing the Ray Optics module.

### 3.1 The COMSOL Modelling Workflow

Briefly the modelling workflow consists of the following steps; illustrated in Figure 3.1, if you start a model completely from scratch:

1. **Initialization of the Model Environment:** Preparing the foundational settings for the simulation.
2. **Geometry Construction:** Designing the model's physical layout.
3. **Material Property Specification:** Assigning specific materials to the model components.
4. **Physics Boundary Conditions Definition:** Establishing the physical constraints and conditions.
5. **Mesh Generation:** Creating the computational grid over the model.

6. **Simulation Execution:** Performing the actual computational analysis.
7. **Results Post-Processing:** Analyzing and visualizing the simulation outcomes.

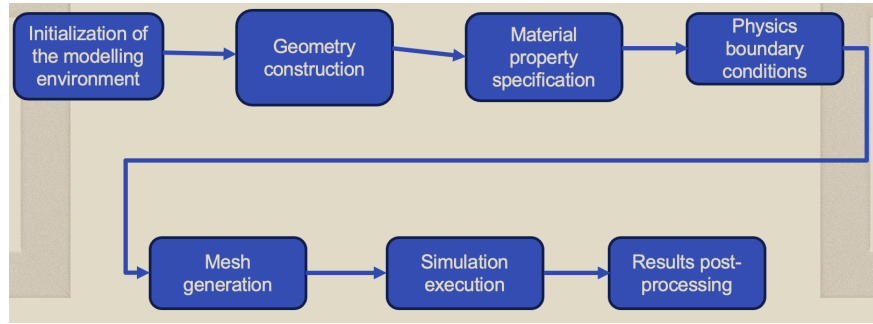


Figure 3.1: The modeling workflow.

In this context, I will demonstrate this workflow first through a simple project, illustrating COMSOL's robust capabilities and the straightforwardness of applying this workflow across various projects, following the sample tutorial given in [3]. It's important to recognize that this workflow remains consistent across different physics simulations, which will guide the development of subsequent models for my thesis.

This demonstration will focus on simulating Joule heating within a busbar, a process where electric current passing through metal results in heating due to electrical resistance.

The busbar in question will incorporate three titanium bolts, with electrical current flowing from a single bolt on one end to a pair of bolts at the opposite end. The objective is to observe the resulting temperature distribution as the busbar undergoes heating.

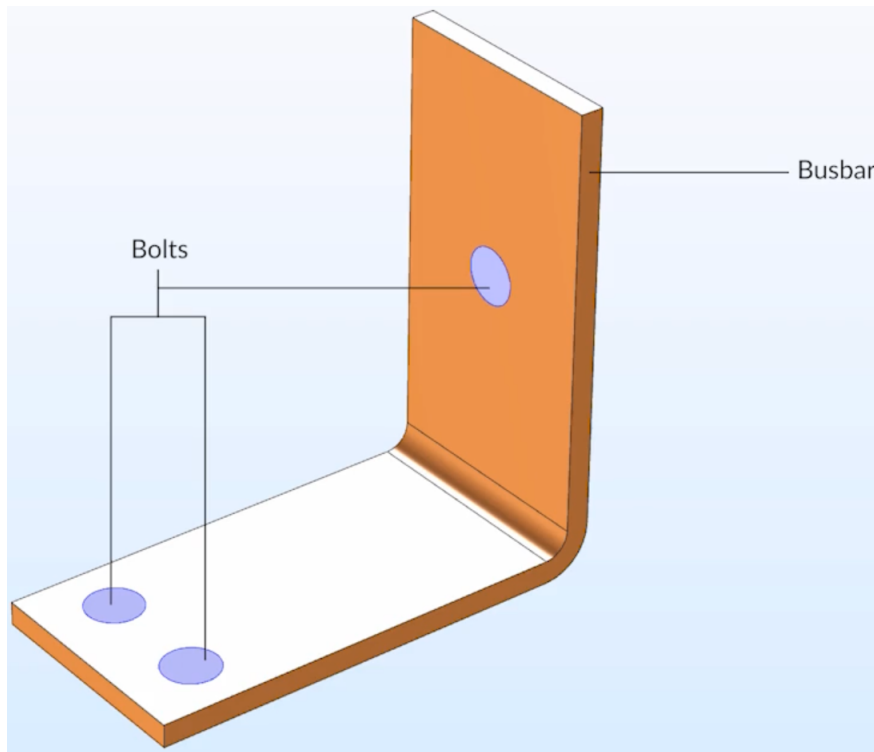


Figure 3.2: The busbar model. Source: [3]

### 3.1.1 Setting Up the Model Environment

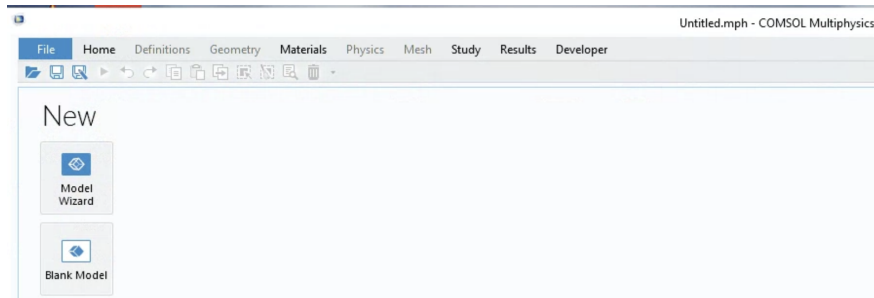


Figure 3.3: Set-up Screen. Source: [3]

Upon launching COMSOL, you are presented with an option to initiate a new project: selecting a Blank Model for starting anew or opting for the Model Wizard for a guided setup. The Model Wizard is advisable for its structured selection process integral to configuring your model. Conversely, choosing a Blank Model grants immediate access to the COMSOL desktop interface, bypassing the preliminary selections required by the Model Wizard.

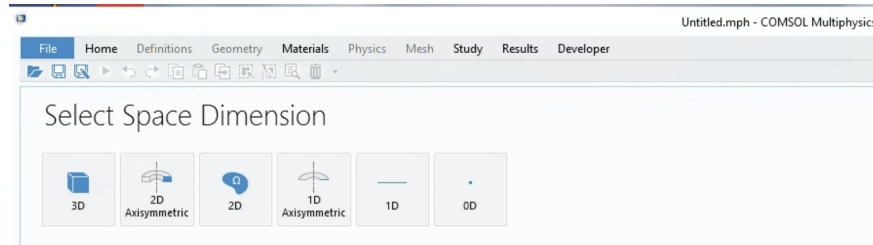


Figure 3.4: Select space dimension screen. Source: [3]

Since our busbar model requires a three-dimensional framework, I select the “3D” option.

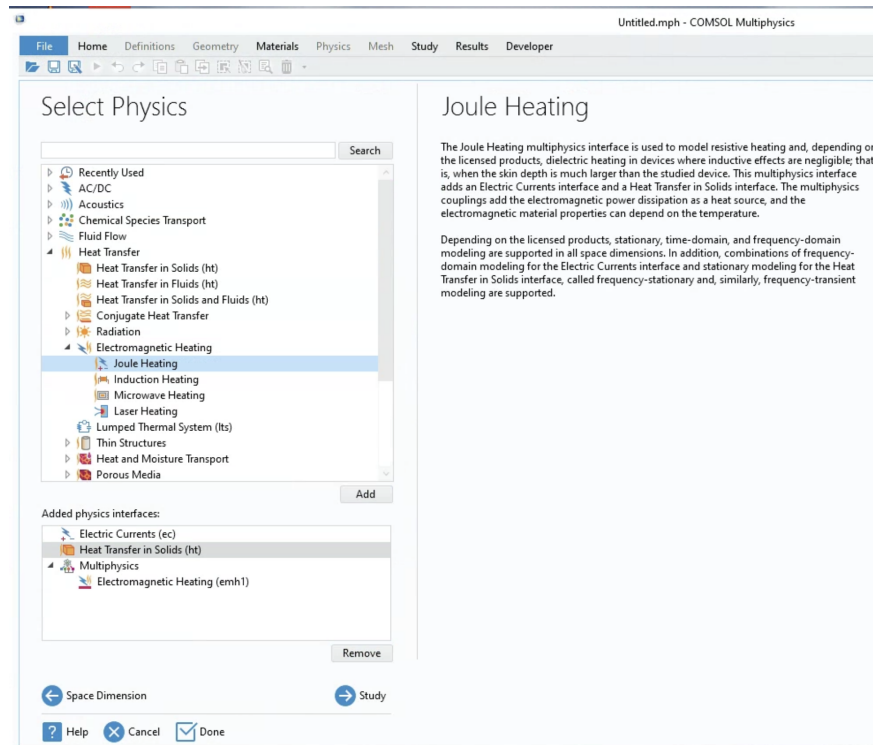


Figure 3.5: Select physics screen. Source: [3]

Subsequently, I arrive at a prompt to select the desired physics for the model. In our case, I opt for Joule heating. In another scenario, for instance, if one’s project was on thin-film fluid flow, navigating to the “Fluid Flow” node and selecting “Thin-Film Flow” would be the procedure. Adding “Joule Heating” automatically associates it with related physics categories like “Electric Currents (ec)” and “Heat Transfer in Solids (ht),” indicating that “Joule Heating” encompasses a composite interface with multiple physics elements integrated.

The selection of physics for exploration significantly hinges on the project’s specific requirements and the level of access provided by your COMSOL subscription. For example,

acquiring the “Ray Optics” module necessary for my thesis entailed a waiting period due to initial subscription limitations. Therefore, early verification of the required physics modules for your project is recommended.

To proceed, I select “Study”.

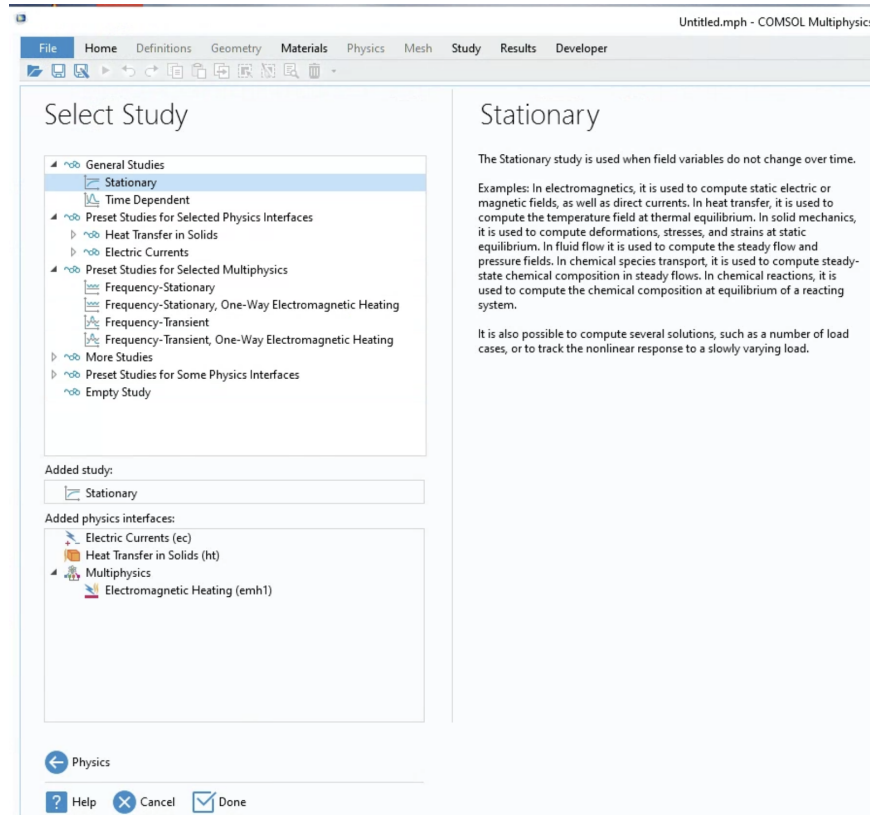


Figure 3.6: Select study screen. Source: [3]

Upon accessing this interface, I am presented with an assortment of study options, determined by our earlier selections regarding the model’s spatial dimensions and physics. For our busbar analysis, the “Stationary” study suffices, given its static nature. After selecting “Done”, I transition to the COMSOL desktop environment.

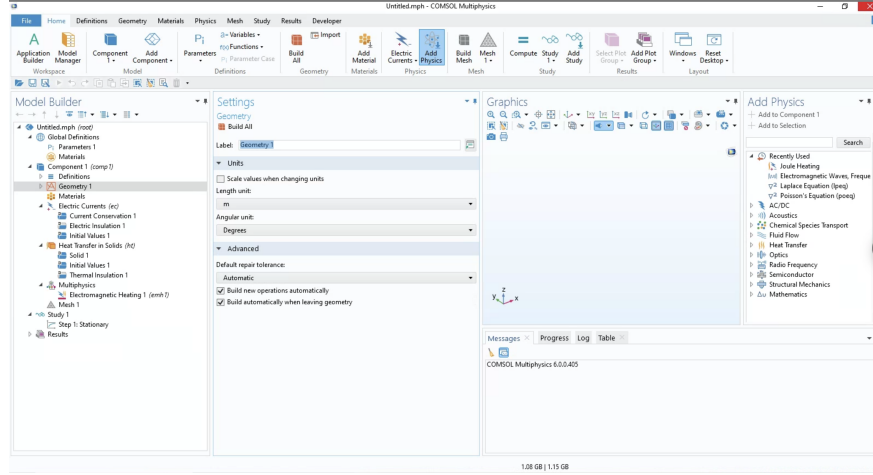


Figure 3.7: The COMSOL desktop. Source: [3]

The COMSOL desktop serves as the central hub for constructing and engaging with your model from the ground up. It is designed with an intuitive interface, featuring buttons and ribbons aligned with the modeling process steps. Within the Model Builder window, you'll find the modeling hierarchy, where you have the capability to define your model's dimensions and select specific physics equations for adherence. Additionally, the layout of the COMSOL desktop windows can be customized to suit your preferences.

### 3.1.2 Building the Geometry

When developing the geometry of your model, multiple pathways are available. You may opt to utilize the drawing tools or geometric shapes provided by COMSOL or import a geometry from an external source.

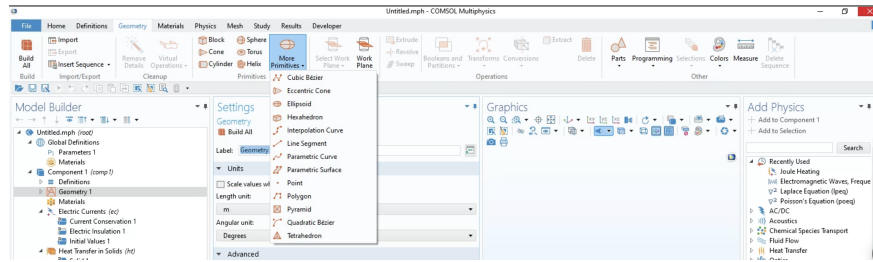


Figure 3.8: Add geometry button selection. Source: [3]

For this instance, given that the busbar geometry already exists within COMSOL's comprehensive library of pre-configured geometries, accessing this resource simplifies the process. This is achieved by navigating to the File menu and selecting Application Libraries.

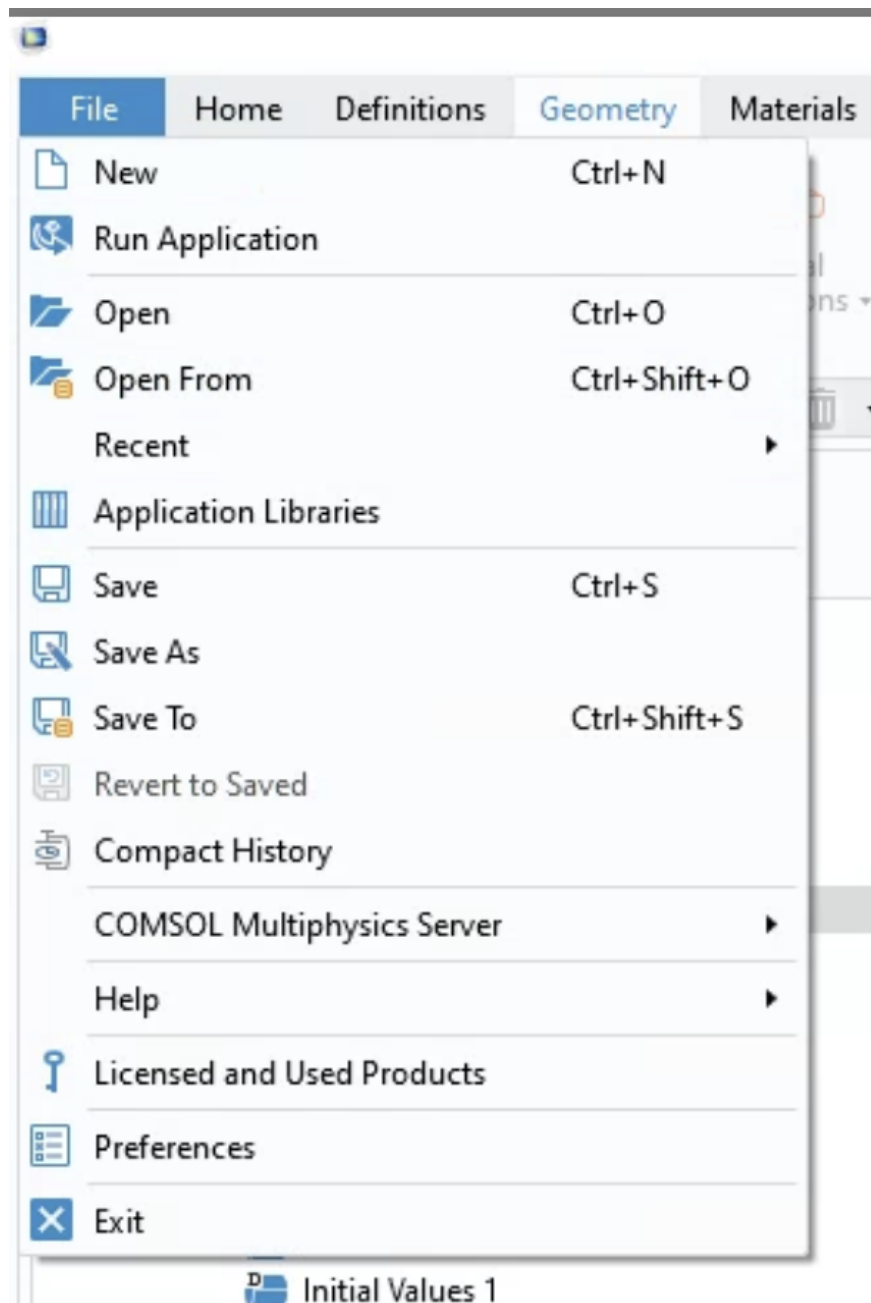


Figure 3.9: Application libraries selection. Source: [3]

Within the Application Libraries, proceed to the COMSOL Multiphysics section, locate the 'busbar\_geom' file, open it, and proceed to save your project accordingly.

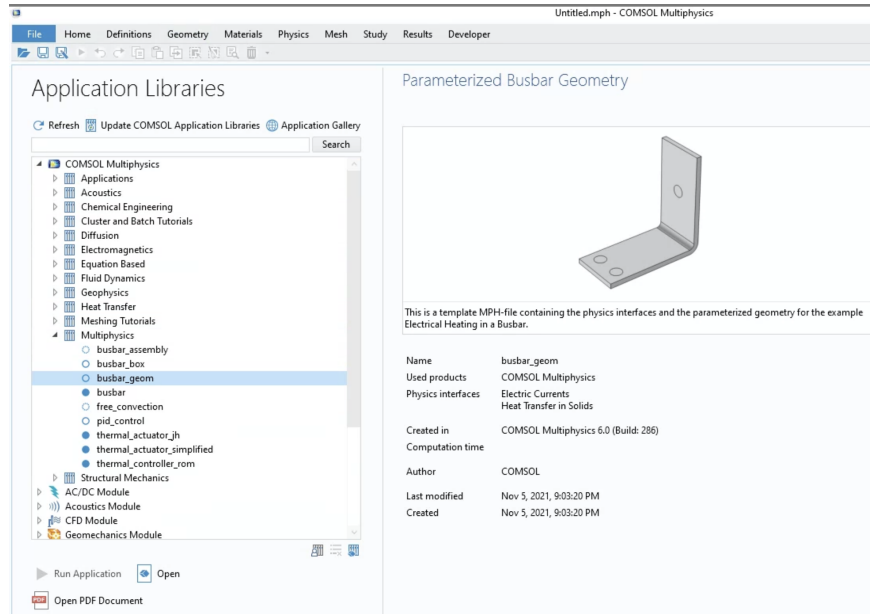


Figure 3.10: Application libraries. Source: [3]

The geometry will now appear in the Graphics window, allowing for zoom and rotational exploration to closely inspect the model. The alteration in the Geometry node within the Model Builder window reflects the sequence of actions executed to construct the busbar geometry. On closer inspection, it becomes evident that specific parameters were employed in crafting this geometry. These parameters are accessible within the “Parameters 1” node, which contains a table detailing the adjustable parameters utilized in the geometry’s creation.

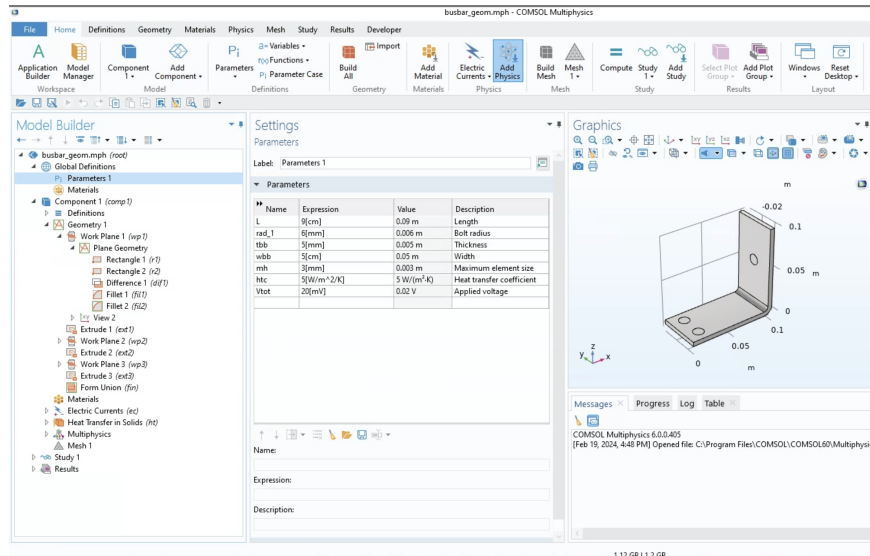


Figure 3.11: COMSOL desktop after adding the busbar geometry. Source: [3]

### 3.1.3 Specifying the Material Properties

Our busbar comprises various components each requiring distinct materials, necessitating batch assignment of materials to selected parts rather than individual allocation. To commence, access the Definitions tab and opt for the Explicit selection.

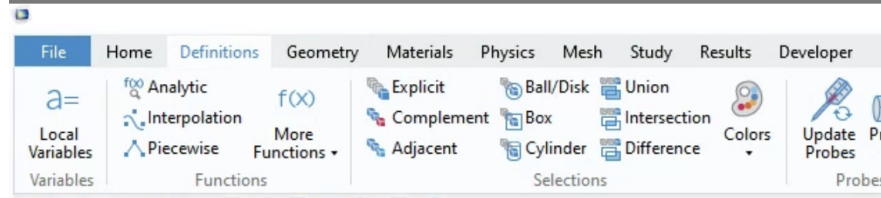


Figure 3.12: Explicit choice from the Definitions tab. Source: [3]

Following this, in the Graphics window, I identify and select the bolts, ensuring both their front and back sides are chosen due to their differing material composition from the busbar's main body.

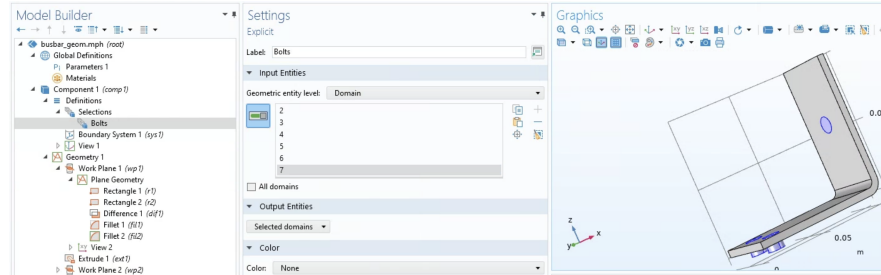


Figure 3.13: Adding bolt selections. Source: [3]

Proceeding to material assignment, I move to the Materials ribbon and select the Add Materials feature. This action opens the “Add Material” window, offering a selection of materials to apply to the chosen components.

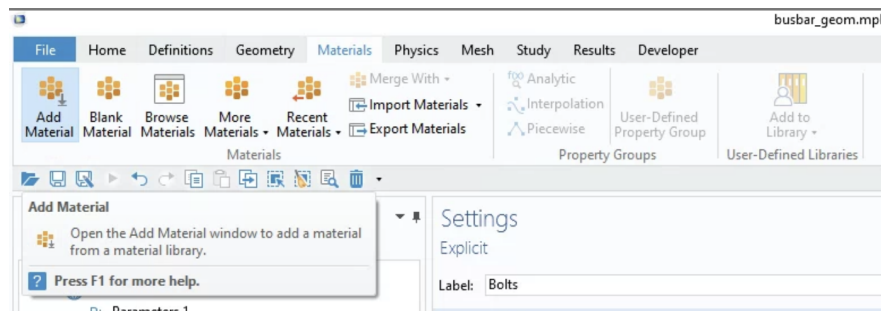


Figure 3.14: Add Materials option from Materials tab. Source: [3]

Select the Built-In option and opt for Titanium (for the bolts) and Copper as the materials.

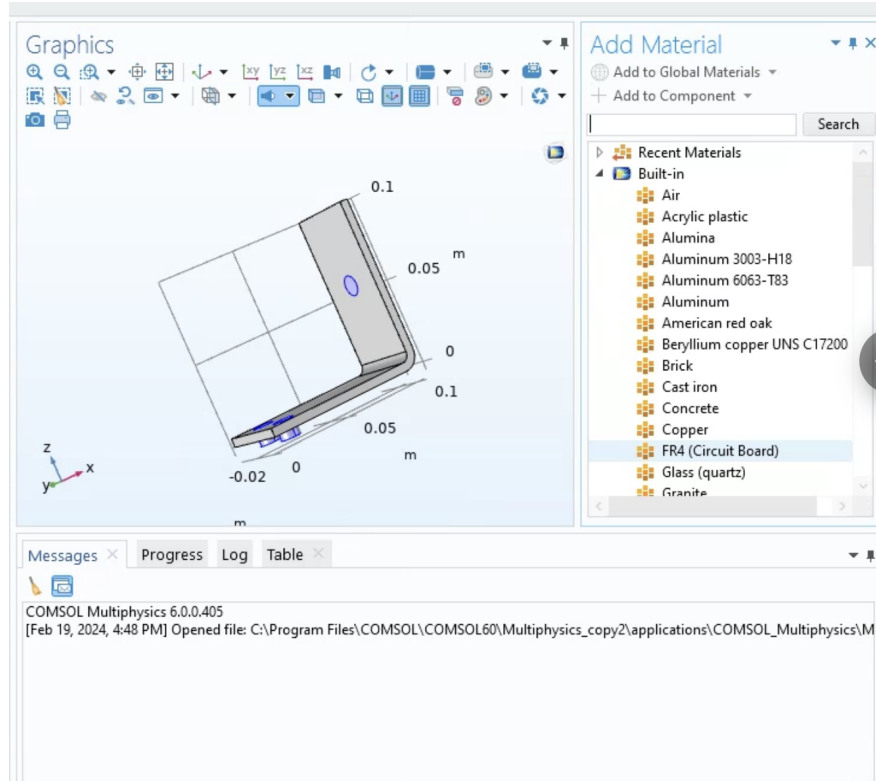


Figure 3.15: Add Materials window. Source: [3]

The earlier defined selection for Bolts proves useful now as I assign Titanium to each bolt by selecting the Bolts option, as illustrated below.

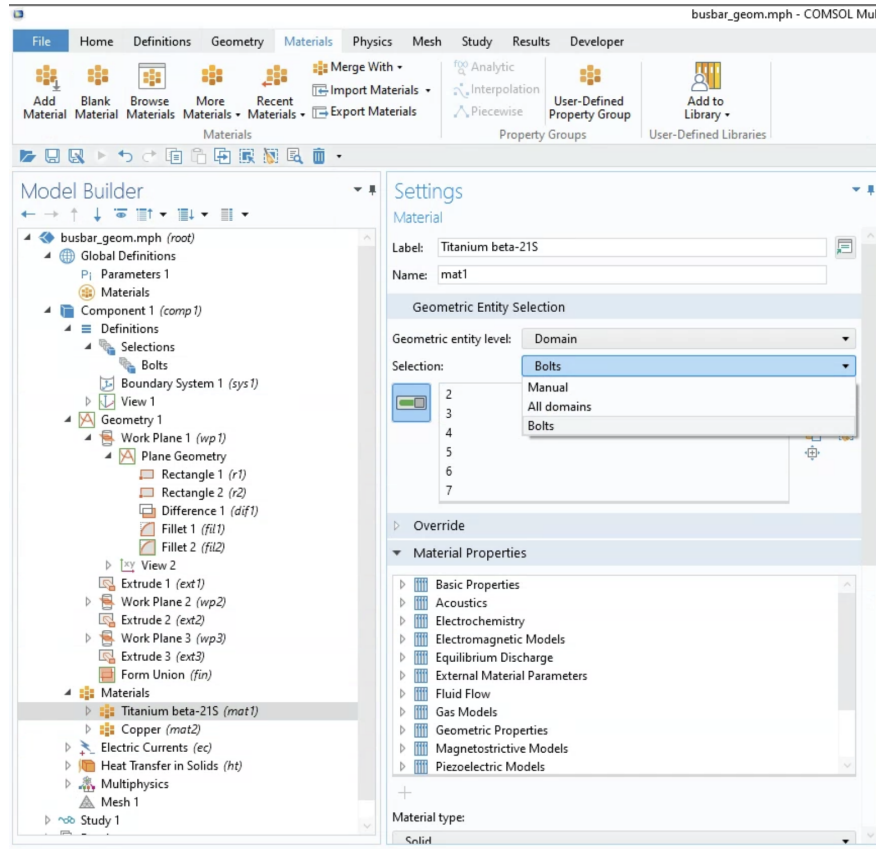


Figure 3.16: Assigning some bolts to be made of Titanium. Source: [3]

Every time a material is added, and consequently a material node is introduced in the Model Builder window, a table appears in the Settings window under Material Contents. This table details the physical properties of the respective materials, including Electrical Conductivity, Heat Capacity, and more.

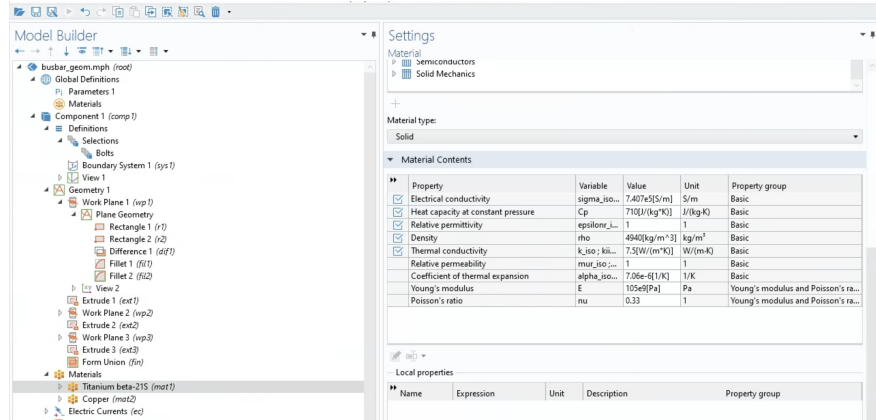


Figure 3.17: Material Properties. Source: [3]

### 3.1.4 Defining the Physics Boundary Conditions

It is time to apply mathematical formulas across various sections of our model to replicate the intended physics. This involves highlighting specific segments of the geometry and imposing relevant formulas and physical parameters that accurately represent those segments.

I will begin by setting up the physics for the electric current interface, aiming to model the flow of electricity from a singular bolt across to the twin bolts at the opposite end of the busbar. The specific physics chosen during the initial model setup might already have certain equations predefined within their physics nodes. For example, within the “Electric Currents (ec)” node, the settings window reveals equations pertinent to this physics. A key equation presented is the fundamental one linking the electric field with electric potential, expressed as  $\mathbf{E} = -\nabla V$ .

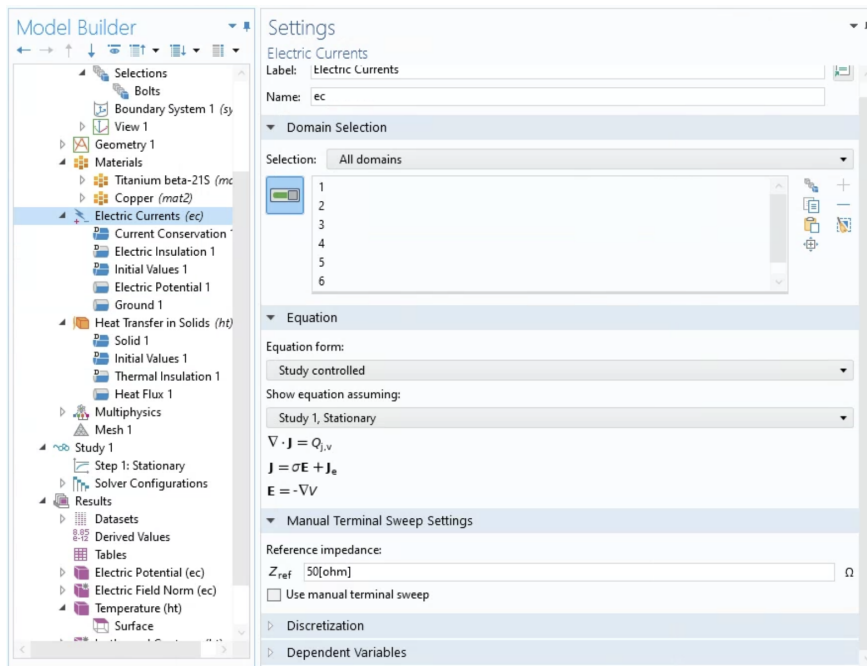


Figure 3.18: The corresponding guiding equation. Source: [3]

COMSOL Multiphysics operates transparently, allowing users to fully grasp the software’s actions and methodologies.

Upon integrating physics into our model, several default nodes were automatically established within each physics category. I add specific boundary conditions and constraints only if they deviate from these defaults. For example, the “Electric Currents (ec)” physics automatically applies the “Electric Insulation 1” condition to all boundaries, which may not suit our model’s requirements.

For our purpose, I aim to impose a voltage on the bottom surface of the single bolt. This is achieved by navigating to the Physics tab, selecting Boundaries, and then choosing Electric Potential. This action adds an “Electric Potential 1” node. The next step is to identify and

select the geometry segment this potential will affect. To specify the electric potential value, I input 20 mV, denoted as 20[mV], with the brackets indicating unit specification.

To simplify the process, remember that the “Parameters 1” node contains a predefined variable,  $V_{tot}$ , representing the applied voltage. Utilizing this variable instead of inputting 20[mV] directly facilitates the setup of parametric studies in the future.

Finally, to complete our setup, I establish a ground boundary condition on the bottom surfaces of the two bolts at the busbar’s opposite end. This is accomplished by selecting Ground from the Physics tab’s boundaries options, then choosing the relevant geometry segments.

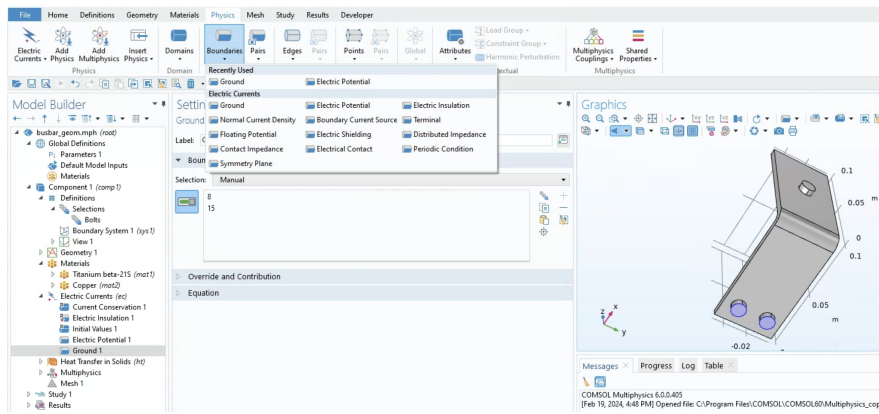


Figure 3.19: Electric Currents boundary conditions. Source: [3]

Given the selection of Joule Heating as a coupled physics in our model, it is essential to define the thermal boundary conditions as well. The default “Thermal Insulation 1” condition, which applies universally across our model, does not suit our specific needs. To address this, proceed to the Physics tab, access Boundaries, and opt for Heat Flux. Within the settings, under Boundary Selection, choose “All Boundaries” but exclude the previously selected bolt surfaces for the Electric Currents boundaries—namely, boundaries 8, 15, and 43—by deselecting these numbers using the “Remove from Selection” option.

For the Heat Flux settings, opt for the “Convective heat flux” under the Flux Type category, entering a value of  $5 \text{ W}/(\text{m}^2 \cdot \text{K})$ . Similar to our approach with the electric potential, revert to the Parameters 1 node and input  $htc$ , which denotes the value of  $5 \text{ W}/(\text{m}^2 \cdot \text{K})$ .

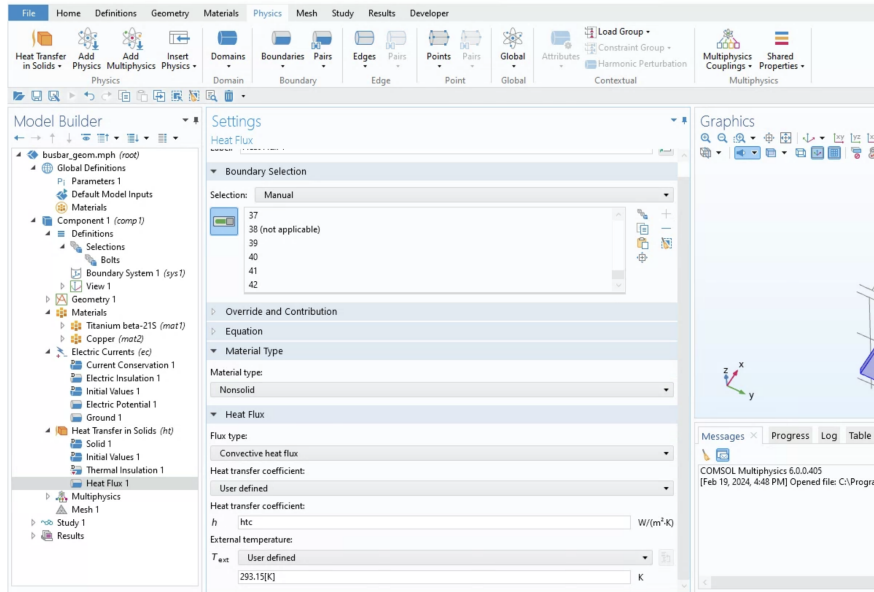


Figure 3.20: Heat Flux boundary conditions. Source: [3]

In our busbar model, the two physics components I have incorporated, namely Electric Currents and Heat Transfer in solids, are universally applicable throughout the model.

### 3.1.5 Build the Mesh

Navigate to the Mesh ribbon and initiate mesh configuration by selecting “Mesh 1.” Within the Settings, under Mesh Setting, accessing the Sequence Type menu presents two alternatives: the default Physics-controlled mesh, which automatically tailors the mesh to the model’s physics requirements, and the user-controlled mesh, granting manual oversight over mesh granularity and enabling the use of diverse element types.

COMSOL Multiphysics accommodates a variety of 2D and 3D element shapes, including pyramids, triangles, and prisms. The software offers nine predefined element size settings, ranging from extremely fine to extremely coarse. To construct the mesh, simply press the “Build All” button.

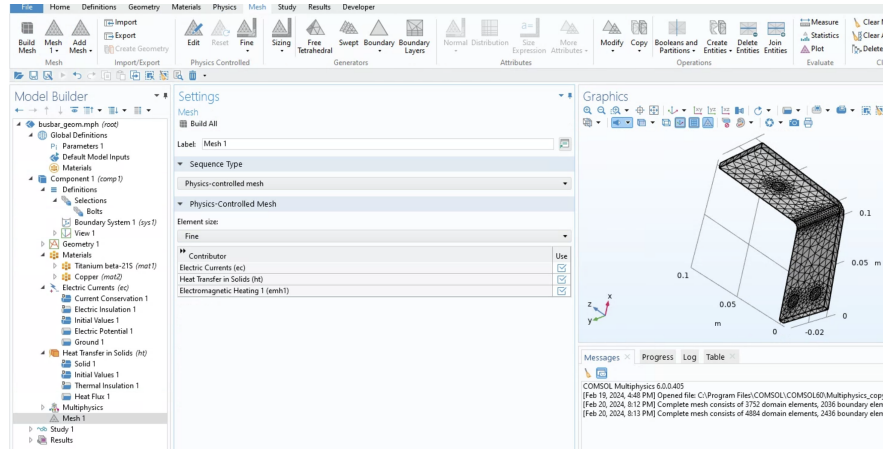


Figure 3.21: Fine mesh type. Source: [3]

### 3.1.6 Run the Study

By selecting and expanding the “Study 1” node within the Settings, there’s an option to “Generate default plots”, which automatically creates visual representations tailored to the physics defined in the model. Given our focus on electric currents and heat transfer, this function will produce plots detailing both the electric potential and the temperature distribution within the busbar.

Under the “Step 1: Stationary” sub-node, found in the “Physics and Variables” dropdown, the integration of the multi-physics problem within the “Solve For” section becomes visible. Proceed by clicking the “Compute” button to perform the simulation. Once computation is complete, the process advances to the next phase, which involves the post-processing of the generated results.

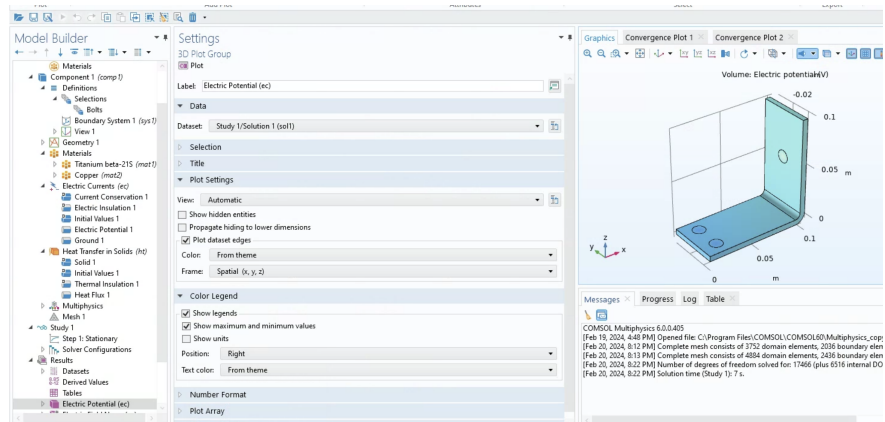


Figure 3.22: Computed results. Source: [3]

### 3.1.7 Post-Processing the Results

The purpose of post-processing in the model construction process is to convert complex simulation data into a user-friendly format that is accessible and informative. The goal is to create a customisable interface using the Application Builder, which is part of COMSOL Multiphysics software. This interface, or simulation application, enables users, often those without extensive simulation background, to explore the model by varying key parameters and instantly visualizing the effects.

Accessible directly from the home toolbar, the Application Builder is an integral tool for enhancing the interactivity and accessibility of the simulation results. The process begins with transforming the busbar model into an interactive application that allows for the modification of predetermined parameters such as the busbar's length, width, and applied voltage.

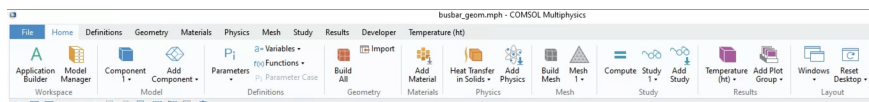


Figure 3.23: Application builder button. Source: [3]

To streamline the creation of the application, I utilize the New Form Wizard, a feature designed for rapid app development within the Application Builder.

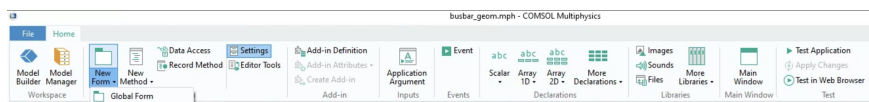


Figure 3.24: New Form Wizard button. Source: [3]

After selecting the adjustable parameters, I then focus on the graphical output that will be displayed in the application and ensure that the user interface includes a 'Compute Study' button to trigger the simulations.

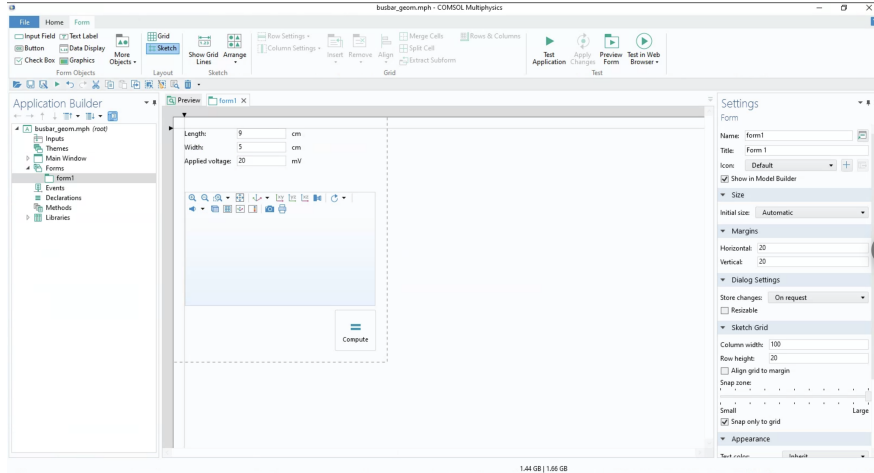


Figure 3.25: Form Editor. Source: [3]

Finalizing the interface through the Form Editor allows me to tailor the application's appearance and functionality to meet user needs. This step is crucial for creating a practical tool that can present complex simulations in an approachable manner.

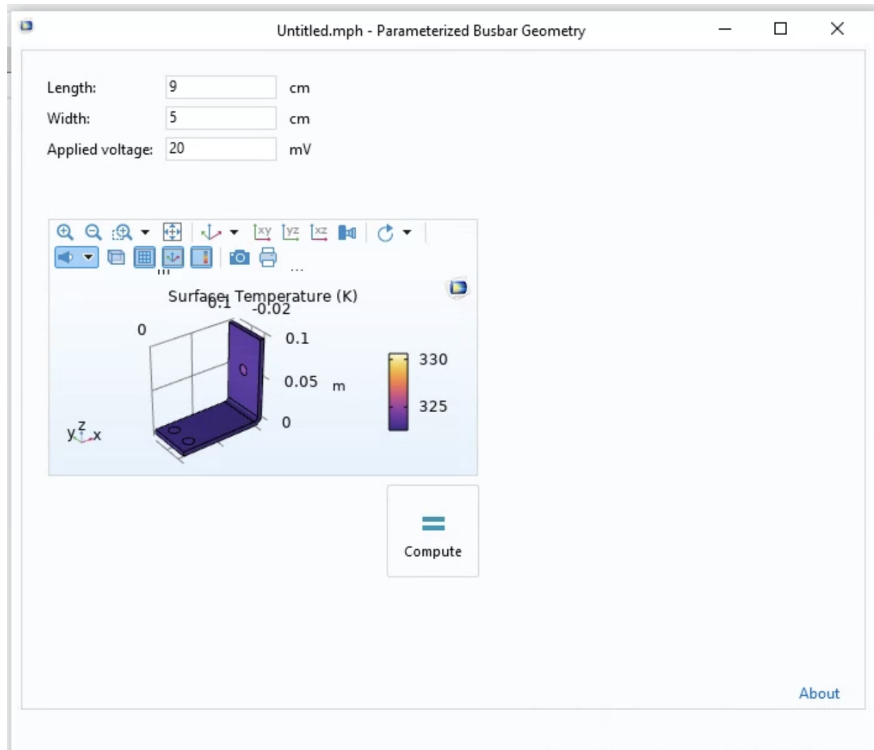


Figure 3.26: Test Application results. Source: [3]

In summary, this chapter outlines a comprehensive guide to the computational methods employed in this thesis, using COMSOL Multiphysics™ to model and simulate the behavior

of optical systems. The detailed workflow, from initializing the model environment to post-processing the results, demonstrates the capability of COMSOL to handle complex multi-physics problems with a user-friendly approach.

Through the application of this workflow, this chapter not only illustrates the modeling of a busbar to simulate Joule heating but also showcases the customization of the application interface, facilitating accessibility for a broader audience.

# Chapter 4

## Computational Results

Embarking on the findings of this chapter, I transition from the established COMSOL modeling workflow to the critical stage of validating theoretical concepts through the lens of computational analysis. The essence of this chapter is twofold: first, to harness the computational prowess of COMSOL in validating key optical phenomena such as anti-reflectivity thus corroborate our simulation outcomes with theoretical models; and second, to attempt to model the simplest Passive Daytime Radiative Cooling devices (PDRCs) at Hudgings Lab by showing how their reflectance varies with wavelength.

My investigation begins with an empirical analysis of anti-reflective behaviors, examining both simple and composite multilayer arrangements. These simulations are meticulously compared to the theoretical predictions presented in *Introduction to Optics* by Frank L. Pedrotti et al. [2].

It is crucial to acknowledge—as delineated in Chapter 2—the analytical derivation of reflectance as a function of angle  $R(\theta)$  and wavelength  $R(\lambda)$  is straightforward for materials with a constant refractive index  $n$ . However, the complexity escalates when dealing with materials where the refractive index varies with  $\lambda$ , a common occurrence in real-world applications. This variation poses significant challenges to traditional analytical methods, thereby necessitating the adoption of sophisticated computational tools like COMSOL for accurate simulations.

We delve into the intricacies of high reflectance by simulating stacks of alternating high and low refractive index layers, shedding light on the nuanced ways layer configurations impact reflectance. These insights are bench-marked against scholarly literature, reinforcing the accuracy of our models.

Moreover, the thesis explores the layered design of PDRCs. By systematically layering silicon, silver, and Polydimethylsiloxane (PDMS), we dissect the optical properties crucial to the development of passive cooling systems. The collection of results and graphs here encapsulate more than just data; they are catalysts for continuous inquiry and deeper understanding of optical physics as it related to PDRCs.

## 4.1 COMSOL: Modeling Anti-Reflectance Coatings

As we progress in our exploration of anti-reflectance coatings, it is beneficial to revisit the foundational principles that govern their behavior. These coatings are designed to minimize reflection and maximize transmission of light through strategic manipulation of refractive indices across different layers.

To appreciate the mathematical underpinnings of these designs, recall a pivotal formula, Equation 2.54, that encapsulates the essence of a two-layer anti-reflecting film's performance. Assuming light strikes normally on the film, the reflectance,  $R$ , can be described by the following relationship:

$$R = \left( \frac{n_0 n_2^2 - n_s n_1^2}{n_0 n_2^2 + n_s n_1^2} \right)^2 \quad (4.1)$$

Here, we anticipate zero reflectance when the expression in the numerator becomes zero, leading us to equation 2.55, which stipulates the condition for achieving no reflectance:

$$\frac{n_2}{n_1} = \sqrt{\frac{n_s}{n_0}} \quad (4.2)$$

This relationship delineates the necessary ratio between the refractive indices of the layers that leads to a reflectance of zero.

When working with a glass substrate of refractive index  $n_s = 1.5$  and air of refractive index  $n_0 = 1$ , the ideal refractive index ratio,  $\frac{n_2}{n_1}$ , is calculated to be  $\sqrt{1.5} \approx 1.225$ .

In COMSOL, our goal is to identify and define (in our parameters table) two materials for the double-layer structure that closely match this ratio to maximize anti-reflective properties. It is crucial to note that the refractive index of most materials varies with wavelength. This variability, known as dispersion, means that optimal thickness and refractive indices for minimizing reflectance at one wavelength may not be as effective at another. While it is challenging to select materials that precisely align their refractive indices to achieve exactly zero reflectance, our aim is to get as close to 0% reflectance over as wide a  $\lambda$  range as practically possible.

The limitation of a quarter-wavelength layer is its selective reflectivity; it effectively eliminates reflection at a specific wavelength but substantially reflects at other wavelengths in proximity. Additionally, its performance varies significantly with the angle at which light strikes the surface. A viable solution to overcome this is the application of multilayer coatings. These coatings, compared to their single-layer counterparts, tend to lower the reflection coefficient over a broader spectrum and accommodate a greater diversity of tangible materials [2].

In the following section, we will compare the reflectivity of two distinct multilayer coatings across an extensive spectral range. The analysis will cover a dual-layer (quarter-quarter wavelength coating) and a triple-layer (quarter-half-quarter wavelength coating). It will be demonstrated that the triple-layer coating achieves a more uniform low reflectance throughout the majority of the visible light spectrum.

### 4.1.1 Anti-reflectance Layers: Setup

The pursuit of anti-reflective coatings leads us to the utilization of thin film dielectrics within COMSOL. In line with the criteria for zero reflectance, the first dielectric film, starting from the base, is cerium trifluoride ( $\text{CeF}_3$ ) with a refractive index of 1.63, while the second film is magnesium fluoride ( $\text{MgF}_2$ ) with a refractive index of 1.38. The refractive index ratio of approximately 1.181 aligns closely with the optimal ratio of 1.225. As established in chapter 2, effective anti-reflectivity for a dual-layer arrangement requires each film to be a quarter-wavelength in thickness, which corresponds to the wavelength at which minimal reflectance is desired.

Note that the anti-reflectance setup below is for normal incidence.

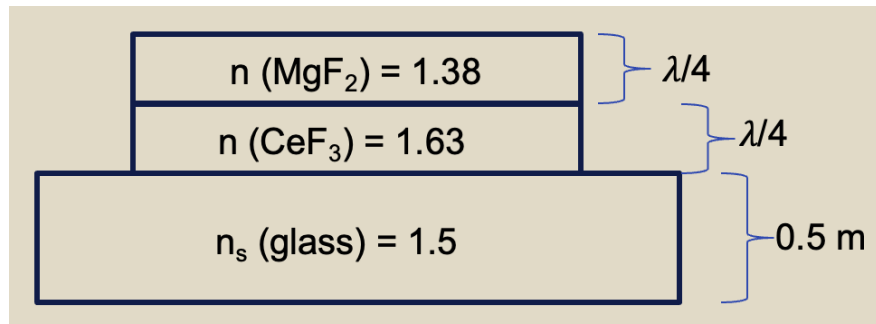


Figure 4.1: The double-layer anti-reflectance coating layout (dimensions not to scale). Source: created by the author using Microsoft PowerPoint.

In our enhanced three-layer structure, designed to broaden anti-reflectivity across a larger wavelength spectrum, the middle layer is a half-wavelength film of zirconium dioxide ( $\text{ZrO}_2$ ), chosen for its refractive index of 2.1. This multi-layer configuration allows for increased anti-reflective performance compared to the more wavelength-specific two-layer model.

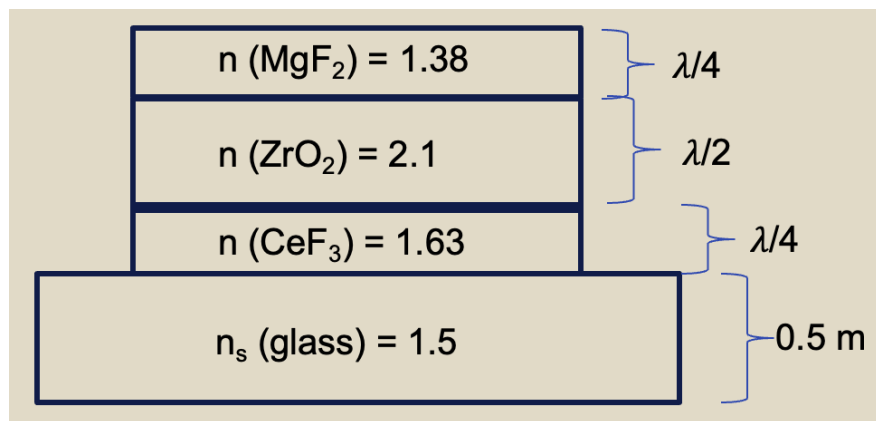


Figure 4.2: The triple-layer anti-reflectance coating layout (dimensions not to scale). Source: created by the author using Microsoft PowerPoint.

This screenshot from the COMSOL desktop highlights the configuration for modeling anti-reflective coatings. Pay particular attention to the 'Film Properties' area within the 'Thin Dielectric Film' settings where the quarter-wavelength calculation is outlined.

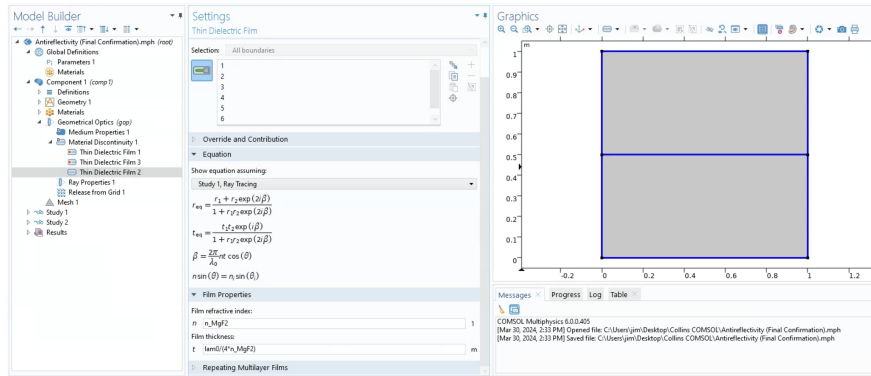


Figure 4.3: COMSOL desktop setup showcasing anti-reflectivity modeling.

Here, the findings from the anti-reflectivity modeling using  $\text{CeF}_3$  and  $\text{MgF}_2$  for the quarter-quarter wavelength combination, as well as  $\text{CeF}_3$ ,  $\text{MgF}_2$ , and  $\text{ZrO}_2$  for the quarter-half-quarter wavelength setup, are presented.

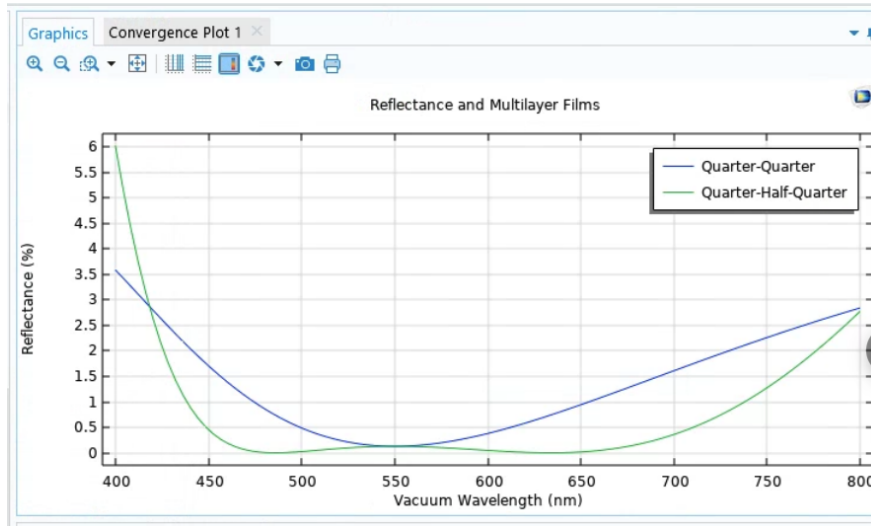


Figure 4.4: Illustration of the reflectance behavior for two anti-reflective coating configurations across the visible light spectrum. The blue line indicates the performance of a quarter-quarter wavelength coating, whereas the green line shows the effect of a quarter-half-quarter wavelength coating.

In the quarter-quarter wavelength design, we employ two layers, each precisely a quarter of the desired wavelength in thickness. While the aim is to achieve minimal reflectance

at a particular wavelength, the actual reflectance seldom reaches absolute zero due to the inherent limitations of material characteristics.

On the other hand, the quarter-half-quarter arrangement introduces an additional layer, half a wavelength thick, nestled between two quarter-wavelength films. This configuration is tailored to minimize reflectance across an extended spectrum of wavelengths.

Such multi-layered coatings surpass the effectiveness of single-layer films for anti-reflective purposes by accommodating a wider wavelength range. This versatility is particularly beneficial in applications where reducing reflection is paramount, such as in the manufacturing of optical lenses.

#### 4.1.2 Verifying Anti-Reflectance Computational Results Through Comparison with Theoretical Optics Literature

This section aims to validate the obtained computational results with the principles outlined in *Introduction to Optics* by Frank L. Pedrotti et al [2].

Beginning with a straightforward approach, we examine the reflectance across various wavelengths for three distinct multilayer film configurations:

1. Films with quarter-quarter wavelength thickness.
2. Films with quarter-half wavelength thickness.
3. Films with quarter-half wavelength thickness, incorporating a different material for the half-wavelength layer.

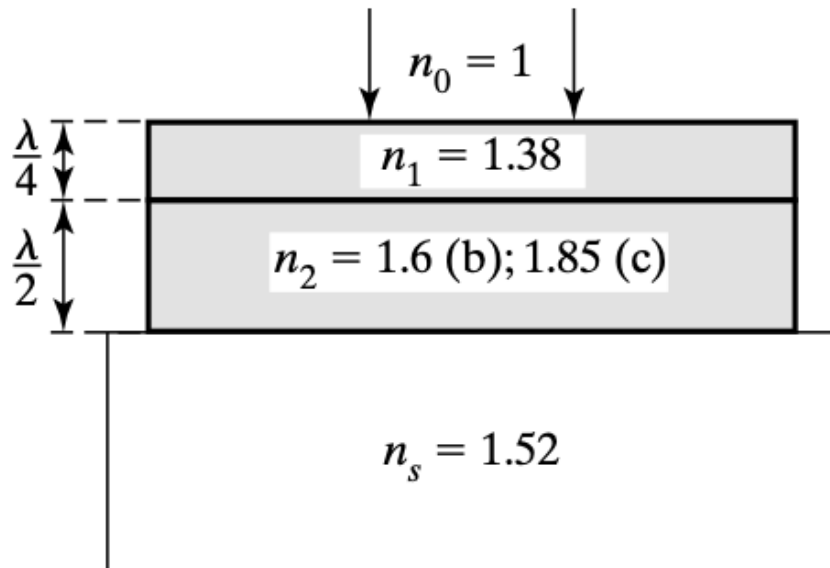


Figure 4.5: Antireflective double-layer arrangement. Source: [2]

We first examine films with quarter-quarter wavelength thickness. The reference from Pedrotti et al. specifies the lower thin dielectric layer as  $\text{ZrO}_2$  and places  $\text{CeF}_3$  directly above. The choice of materials is flexible, provided they adhere to the optimal ratio criterion for anti reflectance as defined in equation 4.2. This results in a refractive index ratio of  $\frac{n_2}{n_1} = \frac{2.1}{1.65} \approx 1.273$ , aligning closely with the ideal ratio of approximately 1.225 for normal incidence, given a substrate refractive index ( $n_s$ ) of 1.5.

Expanding the spectrum of low reflectance within the visible region becomes achievable by diverging from the constraint of equal quarter-wavelength ( $\lambda/4$ ) coatings. By integrating a layer of quarter-wavelength thickness as the second layer (considered from the bottom upwards), we attain more extensive zones of diminished reflectance. Consequently, in the scenario of item 2, we employ magnesium fluoride ( $\text{MgF}_2$ ), characterized by a refractive index of 1.38, as the quarter-wavelength thick material. The intermediate half-wavelength layer utilizes aluminum oxide, with a refractive index of 1.60. For item 3, thorium dioxide, featuring a refractive index of 1.85, serves as the material for the half-wavelength thick layer, as noted in [2].

For the specific wavelength of 550 nm, where the thicknesses of the quarter-wavelength ( $\lambda/4$ ) and half-wavelength ( $\lambda/2$ ) layers are calculated, the half-wavelength layer does not influence reflectance. In this case, the double-layer system acts akin to a solitary quarter-wavelength layer, resulting in a reflectance of 1.3%. At wavelengths close to 550 nm, the presence of the half-wavelength layer contributes to maintaining reflectance levels below those achieved by a two quarter-wavelength layers. Below is the plot illustrating reflectance against wavelength for scenarios 1 through 3.

The graph below illustrates anti-reflectivity trends as detailed in the Optics textbook, indicating that while the reflectance at a wavelength of 550 nm stands at approximately 1.3%, this value surpasses the performance of the quarter-quarter wavelength coating. Nevertheless, reflectance stays below this threshold across a wide wavelength span, extending from roughly 420 to 800 nm. This suggests that alternative configurations for dual-layer reflective films could be viable if the layers are not strictly constrained to quarter-wavelength multiples.

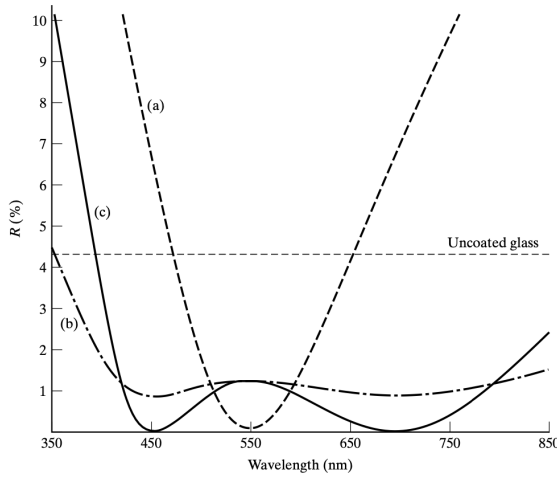


Figure 4.6: Anti-reflectance graphs as shown in the optics textbook.

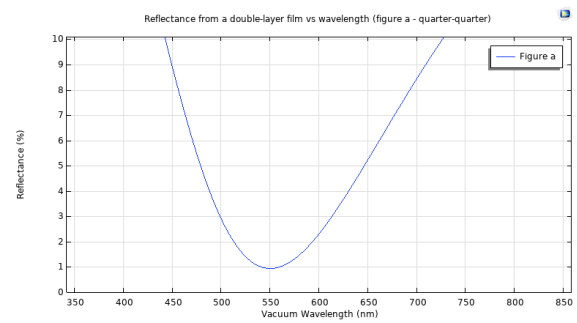


Figure 4.7: Anti-reflectance coating with 2 layers, each a  $\lambda/4$  thick.

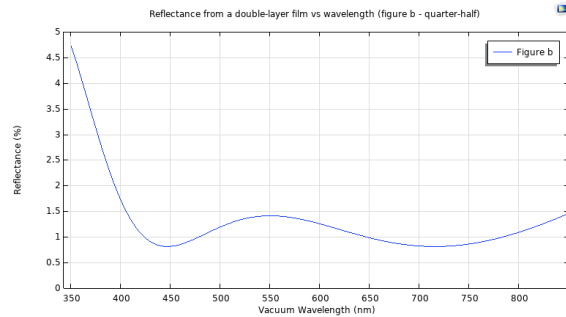


Figure 4.8: Anti-reflectance coating with  $\lambda/4$  thick bottom layer and  $\lambda/2$  thick top layer of  $n = 1.6$



Figure 4.9: Anti-reflectance coating with  $\lambda/4$  thick bottom layer and  $\lambda/2$  thick top layer of  $n = 1.85$

These results derive from the principles outlined in Chapter 2. Initially, the overall transfer matrix elements are calculated by multiplying the transfer matrices of the individual layers together. Within these calculations, the phase difference,  $\delta$ , varies with  $\lambda$ , aligning the film thickness with either  $\lambda/4$  or  $\lambda/2$  at the reference wavelength of 550 nm.

Subsequently, the reflection coefficient, as outlined in 2.51, is squared to produce reflectance as a wavelength function. COMSOL's Ray Optics module significantly simplifies this process by automating several steps, although careful consideration is needed for layer treatment, particularly regarding their classification as thin dielectric films.

## 4.2 COMSOL: Modeling High Reflectance.

To achieve anti-reflective properties, layers are arranged starting from the air and progressing through low-index to high-index materials before reaching the substrate. In contrast, for

enhanced reflectivity, the sequence is reversed, starting from the air to high-index and then to low-index materials before ending at the substrate. This arrangement encourages multiple reflections of the incident light within the layered structure.

A combination of layers arranged to maximize reflectivity is known as a *dielectric mirror*, *high-reflectance stack*, or *distributed Bragg reflector*. It's important to note that achieving high reflectance across the solar spectrum is a key factor for effective passive daytime radiative cooling, as previously discussed.

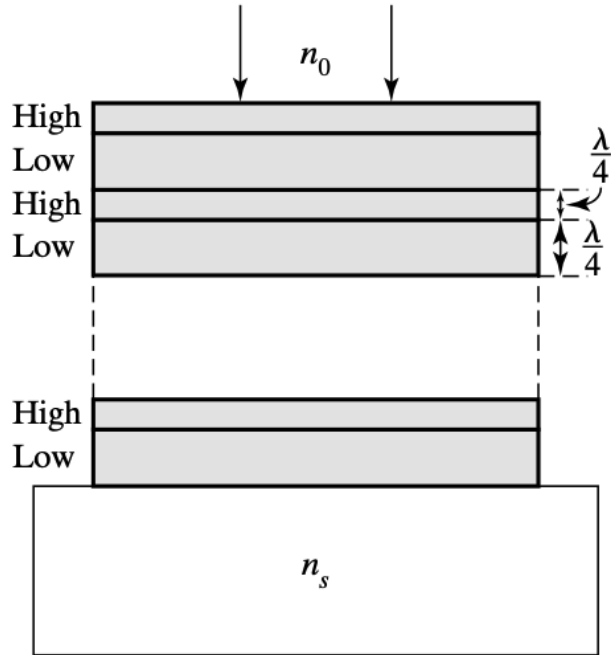


Figure 4.10: High-reflectance stack comprising double layers with alternating high and low refractive indices. Source: [2]

#### 4.2.1 Verifying High Reflectance Computational Results Through Comparison with Theoretical Optics Literature

The formula to ascertain high reflectance,  $R$ , at a chosen design wavelength ( $\lambda_0$ ) for a specific layer arrangement is denoted by 2.58.

$$R = \left[ \frac{\left( \frac{n_0}{n_s} \right) \left( \frac{n_L}{n_H} \right)^{2N} - 1}{\left( \frac{n_0}{n_s} \right) \left( \frac{n_L}{n_H} \right)^{2N} + 1} \right]^2 \quad (4.3)$$

Achieving maximal reflectance (100%) occurs under the following conditions:

1. As  $N$ , representing the count of layer pairs, becomes very large.

2. When the ratio  $\frac{n_L}{n_H}$  approaches zero.

The optics textbook illustrates high reflectance with the following depiction:

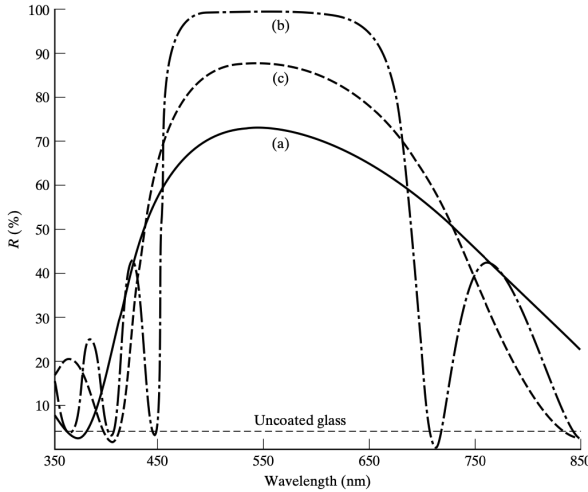


Figure 4.11: Reflectance spectra for high-low index stacks: (a) for a two-layer double stack, (b) for a six-layer double stack, and (c) for a two-layer double stack enhanced with an additional high-index layer at the very top. Source: [2]

In these configurations, layers are designed to be  $\lambda/4$  thick at a design wavelength  $\lambda_0 = 550$  nm. Here, the high-index material (Zinc Sulfide - ZnS) has  $n_H = 2.35$ , the low-index material (Magnesium Fluoride - MgF<sub>2</sub>) has  $n_L = 1.38$ , and the incident medium (air) has  $n_0 = 1.00$ . The ratio of  $\frac{n_L}{n_H}$  is thus approximately  $\frac{1.38}{2.35} \approx 0.587$ .

Our analysis will specifically address graph (c), which demonstrates how adding an extra high-index layer between the substrate and the final low-index layer enhances maximum reflectance in a two-layer double stack ( $N = 2$ ). This addition improves reflectance efficiency compared to simpler two-layer double configurations.

The findings showcased below stem from applying the high reflectance principles discussed in Chapter 2. Observe the alignment of peak reflectance with the textbook's findings, achieving 90%.

Employing a parametric sweep in COMSOL allows for the exploration of reflectance variation across wavelengths by systematically adjusting the count of double layer pairs ( $N$ ) to values such as 2, 5, 10, and 20. This approach calculates solutions across a range of parameter sets. For all depicted graphs, an extra top layer with a high refractive index is incorporated to broaden the spectrum of maximum reflectance.

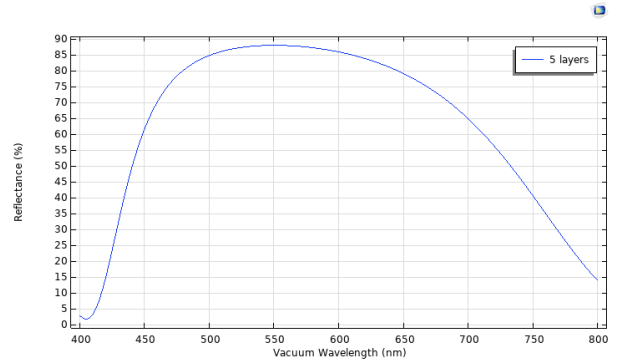


Figure 4.12: Spectral reflectance for a structure with two pairs of high-low refractive index layers, topped with an additional high-index layer. This figure is similar to plot (c) present in the left figure.

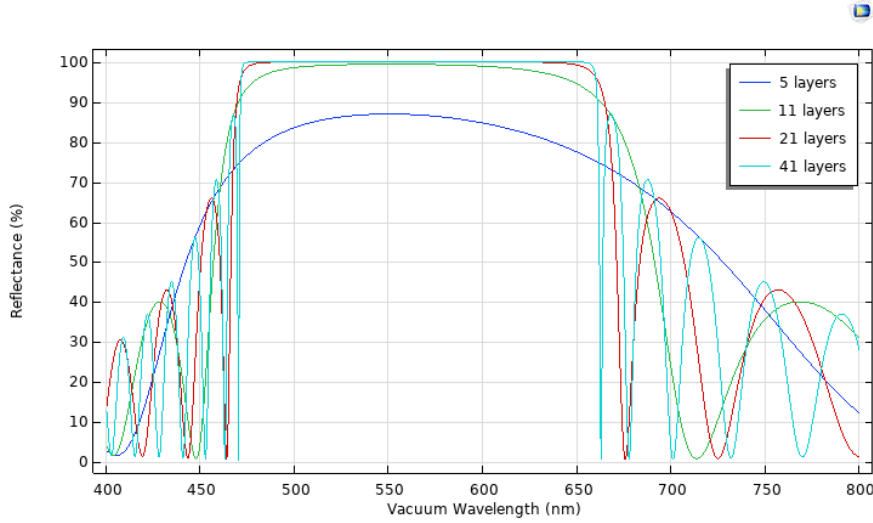


Figure 4.13: Reflectance comparison for configurations with 5, 11, 21, and 41 layers, each enhanced by an additional high-index surface layer.

Unlike conventional metallic mirrors, DBRs leverage a careful and simple engineered structure of alternating thin layers of materials with contrasting refractive indices. This design typically features an odd number of layers, anchored by high refractive index materials at both ends, optimizing their reflectivity [11].

At the core of a DBR's functionality is the concept of constructive interference. As optical waves encounter the boundaries between layers, each boundary induces a partial reflection. When the optical wave's wavelength is four times the layers' optical thickness, these reflections interfere constructively, transforming the layers into an efficient reflector. This principle gives rise to a *stopband*, a wavelength range where the reflector achieves heightened reflection. With an adequate number of layers, a DBR can achieve a high-quality reflection, making it useful in the operation of vertical cavity surface emitting lasers [11].

Expanding beyond the *stopband*, DBRs exhibit a characteristic where reflectance transitions into a pattern of oscillating maxima and minima. By strategically adjusting these parameters, it is possible to shift the stopband's center, enhancing the filter's spectral transmittance across a broader range. This capability to finely control the light's passage through these structures not only underscores the versatility of DBRs but also paves the way for their integration into a wide array of optical devices, where precise manipulation of light is paramount [2].

### 4.3 COMSOL: Modeling PDRCs

At Hudgings Lab, one of the foundational PDRC designs comprises a straightforward sequence of layers. Beginning with silicon as the foundation, a layer of silver is applied directly above, topped with a final layer of Polydimethylsiloxane (PDMS).

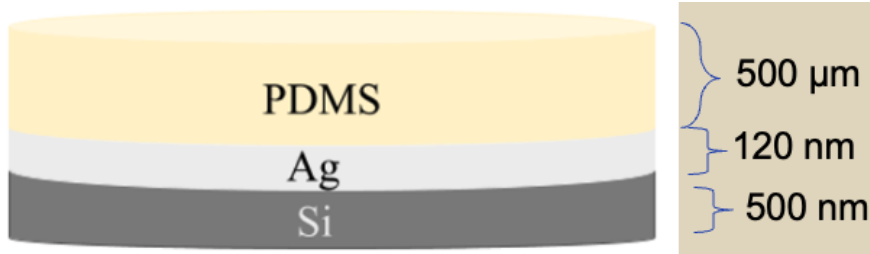


Figure 4.14: Illustration of a basic PDRC configuration at Hudgings Lab, featuring a silicon base with subsequent layers of silver and PDMS.

To understand the optical behavior of this structure, I systematically approached the modeling process from the bottom layer upwards. The following results present a sequence of reflectance versus wavelength analyses for each layer configuration: initially for silicon, followed by silicon with an added silver layer, and concluding with the composite structure of silicon, silver, and PDMS. This progression illustrates how each layer contributes to the overall reflectance spectrum.

### 4.3.1 Analysis of Silicon Layer Only

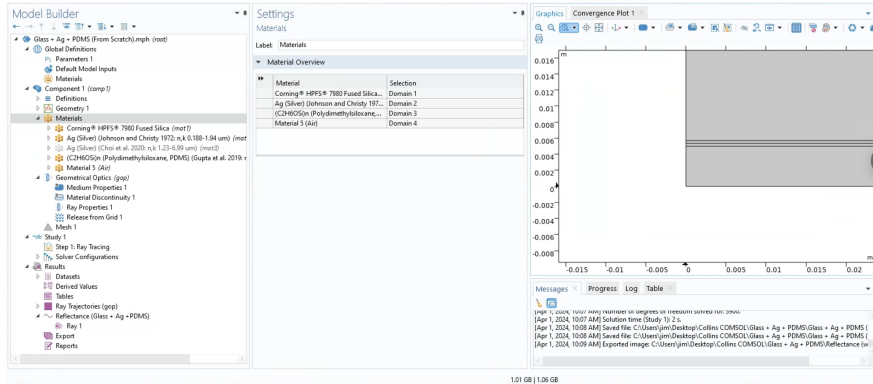


Figure 4.15: COMSOL desktop setup for PDRC analysis demonstrating the simulation framework.

For simulations that span across various wavelengths, it is crucial to include the wavelength-dependence of the refractive indices of our materials. COMSOL tabulates  $n(\lambda)$  for specific  $\lambda$  measured in the literature. Then it interpolates between these experimentally measured points. This method allows for dynamic adjustment of a material's refractive index in response to changes in wavelength during simulations, providing a more accurate representation of the material's optical behavior.

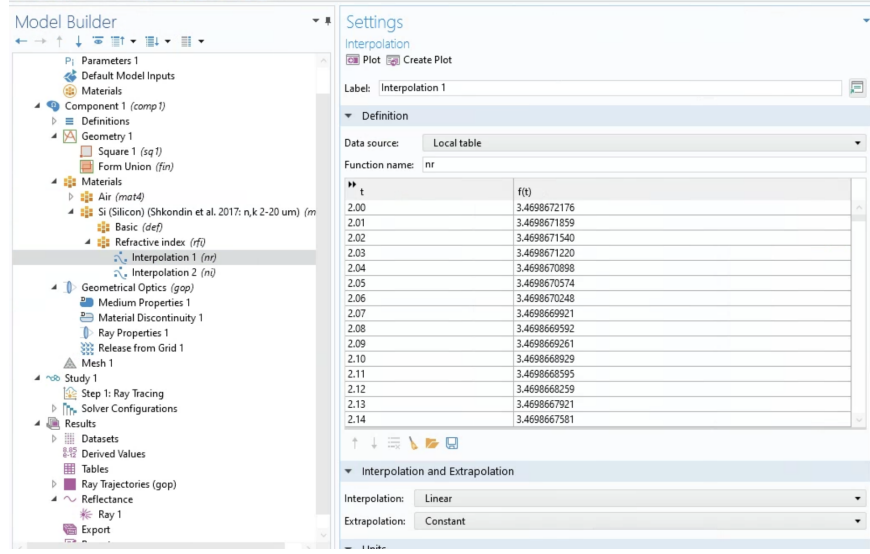


Figure 4.16: Interpolation table for the silicon substrate, showing the wavelength-dependent refractive index.

Utilizing the interpolation table enables the plotting of an interpolation function, offering a graphical representation of how refractive indices fluctuate with wavelength. This capability enriches the COMSOL simulation by providing a more precise depiction of light-material interaction over diverse wavelengths, a critical aspect in optics where dispersive phenomena play an important role.

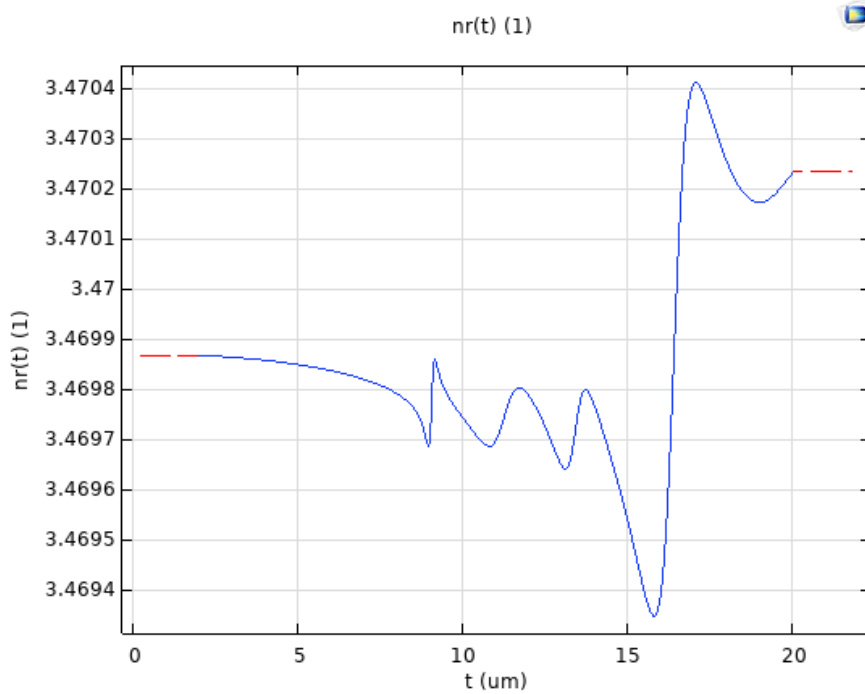


Figure 4.17: Interpolation plot for the silicon substrate, showing the wavelength-dependent refractive index.

For this reason, I selected (*Silicon*) (*Shkondin et al. 2017: n,k 2-20 um*) for the substrate, taking advantage of its accompanying interpolation function. It is vital to acknowledge that interpolation functions, which depict the wavelength-dependent refractive index variations of materials, can also be derived from experimental data found in scientific literature.

When generating a reflectance versus wavelength graph using only the silicon substrate, the reflectance indeed shows variation across different wavelengths.

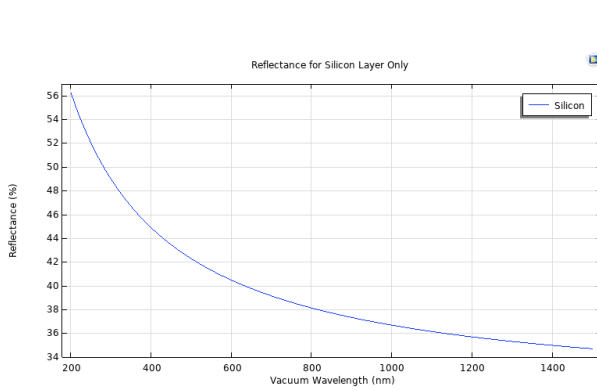


Figure 4.18: Reflectance variation with wavelength for (Silicon) (Shkondin *et al.* 2017:  $n, k$  2-20  $\mu\text{m}$ ).

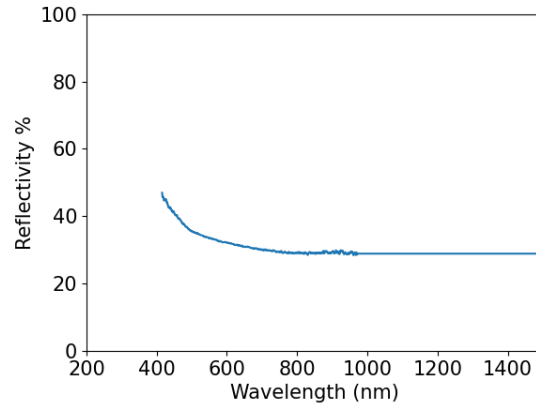


Figure 4.19: Reflectance variation with wavelength for Silicon, experimentally measured by Fernando Castillo at Hudgings Lab. Measurements were taken at a 10-degree angle from the normal.

Within the displayed wavelength range, a sole substrate yields a reflectance below 45% within the visible spectrum, which falls short of the desired high reflectivity within the solar spectrum for optimal PDRC performance. This observation underscores the need for integrating materials capable of meeting the dual objectives of high solar reflectance and substantial emissivity within the atmospheric window.

Focusing initially on enhancing solar reflectance, designs at Hudgings Lab incorporate silver on top the substrate due to its exceptional reflectivity in the solar spectrum. Having illustrated the outcomes with merely the glass substrate and underscored the importance of a highly reflective layer in the solar spectrum, I will venture into simulating the combined effects of glass and silver layers.

### 4.3.2 Analysis of Silicon plus Silver Layers

Next, I added a silver layer on top the silicon substrate, recognizing the continued necessity for an interpolation function to accurately represent silver's refractive index across various wavelengths.

COMSOL offers a comprehensive collection of silver materials, each accompanied by interpolation tables that chart the refractive indices over preferred wavelength spans. The entry *Ag (Silver)* (Ciesielski *et al.* 2017:  $Ag/SiO_2$ ;  $n, k$  0.191-20.9  $\mu\text{m}$ ) provides data on silver's refractive indices from 0.191 to 20.9 ( $\mu\text{m}$ ), where  $n$  is the real component of the complex refractive index and  $k$ , the extinction coefficient, is the imaginary part, indicating the material's degree of light absorption.

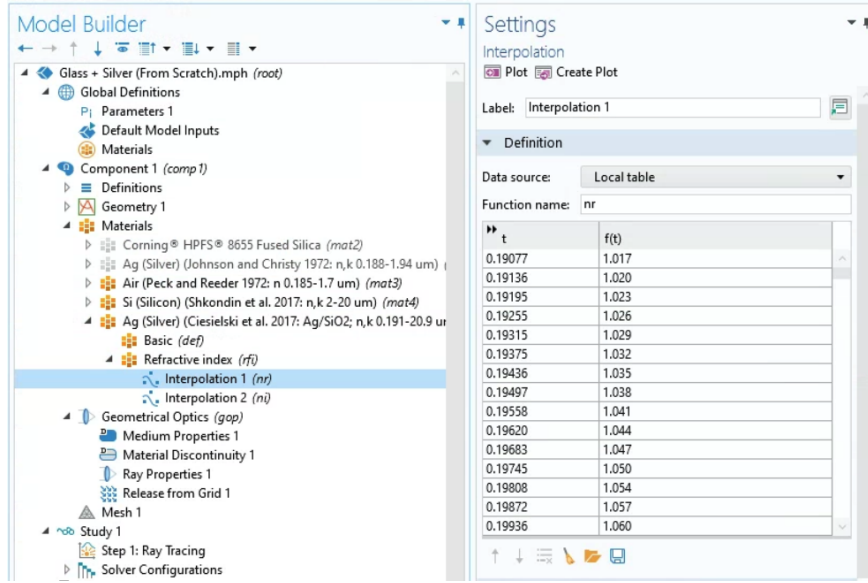


Figure 4.20: Interpolation table for silver's refractive index.

The figure below displays a plot of the refractive index interpolation of *Ag (Silver)* (*Ciesielski et al. 2017: Ag/SiO<sub>2</sub>; n,k 0.191-20.9 um*).

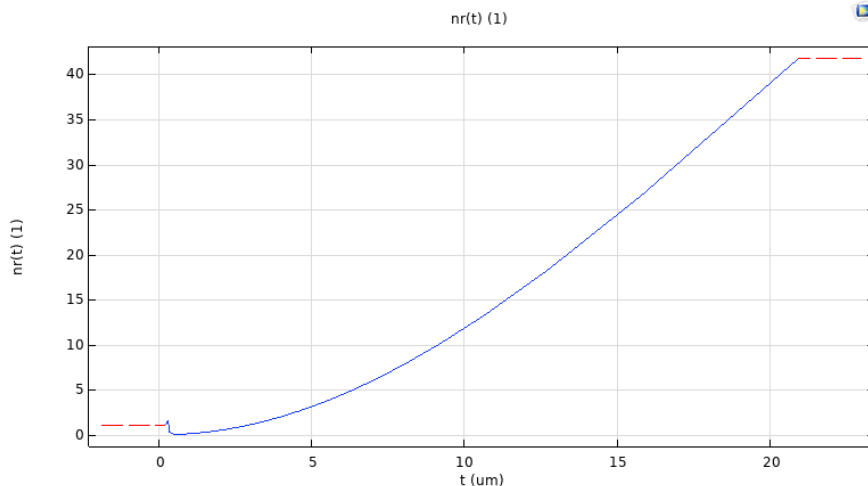


Figure 4.21: Interpolation plot for silver's refractive index.

The figures below display the reflectance outcomes utilizing *Ag (Silver)* (*Ciesielski et al. 2017: Ag/SiO<sub>2</sub>; n,k 0.191-20.9 um*).

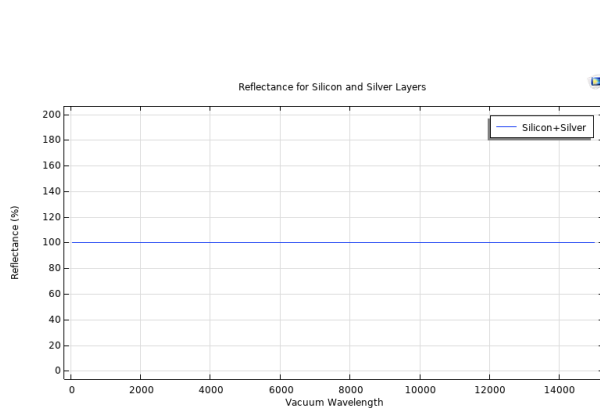


Figure 4.22: Reflectance results for Silicon and Silver Layers

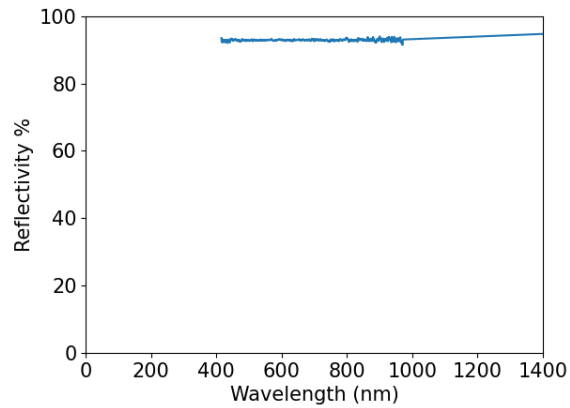


Figure 4.23: Reflectance variation with wavelength for silicon and silver, experimentally measured by Fernando Castillo at Hudgings Lab. Measurements were taken at a 10-degree angle from the normal.

These graphs mostly reflect the expected outcomes. Given silver's high reflectivity across the visible wavelength spectrum, we observe near 100% reflectance within the visible range (400 - 700 nm).

### 4.3.3 Analysis of Silicon plus Silver plus PDMS Layers.

In the final step, a PDMS layer was applied on top of the silver layer. This step also utilized a PDMS material equipped with a pre-defined interpolation function for its refractive index, specifically  $(C_2H_6OSi)_n$  (Polydimethylsiloxane, PDMS) (Gupta *et al.* 2019:  $n$  0.30-1.69  $\mu m$ ).

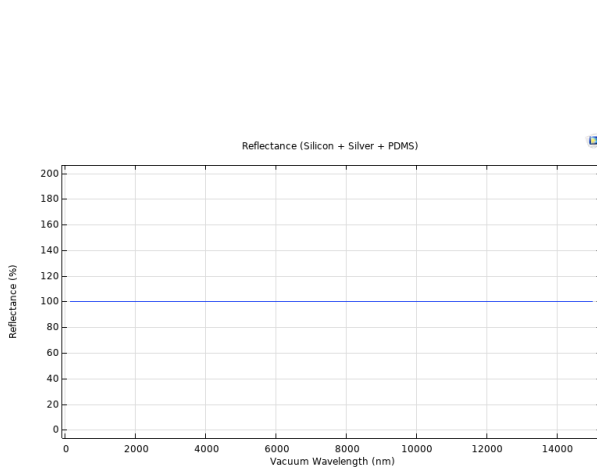


Figure 4.24: Reflectance analysis for a composite of silicon, silver, and PDMS.

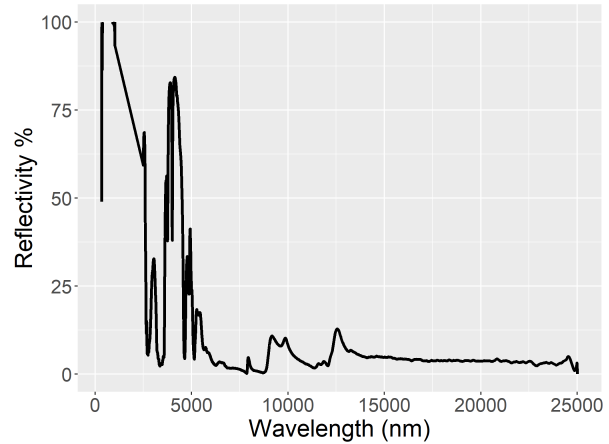


Figure 4.25: Reflectance variation with wavelength for silicon, silver, and PDMS layers, as experimentally determined by Fernando Castillo. The reflectance measurements were conducted at an angle of 10 degrees from the normal.

This setup achieved a peak reflectance of 100% across a broad wavelength range. However, as illustrated in Figures 4.24 and 4.25, the figures do not align perfectly, indicating that further work is needed in this area but one prevailing clue could be that the PDMS layer does not affect the reflectance that much in the visible spectrum. Indeed, the purpose of the PDMS is to enhance emissivity in the atmospheric window. See Figure 1.3.

We conclude our examination of optical phenomena using COMSOL. This chapter had two aims: first, to validate theoretical concepts like anti-reflectivity and high reflectance using COMSOL, and second, to initiate the simulation of basic PDRC configurations as designed at Hudgings Lab.

We began by evaluating anti-reflective strategies, ranging from simple to complex multilayer systems, against theoretical predictions from *Introduction to Optics* by Frank L. Pedrotti et al. This comparison affirmed the accuracy of our simulations. Additionally, we modeled PDRC devices by layering silicon, silver, and Polydimethylsiloxane (PDMS), revealing key optical properties essential for passive cooling effectiveness.

This chapter demonstrates the synergy between theoretical physics and computational modeling, offering a solid foundation for future research to expand upon. It underscores the importance of simulation in confirming theoretical models and opens avenues for improving PDRC device design.

Looking forward, the results from this chapter not only validate our understanding of optical principles but also suggest strategies for enhancing PDRC performance through material and design optimization.

# Chapter 5

## Conclusion

The initial chapters laid the groundwork by illustrating the critical role of cooling technologies in addressing the pressing issues of global warming and the energy crisis. With an emphasis on PDRCs, we embarked on a journey through the theoretical underpinnings and practical applications of these devices, which offer the potential for efficient, energy-free cooling by radiating heat directly to outer space during daylight hours.

As we culminate this research, this concluding chapter aims to distill the insights gained from our investigations, outlining the contributions of this work to the field of cooling technologies and the broader context of sustainable energy solutions.

### 5.1 My work

COMSOL Multiphysics™ has proven itself as an indispensable tool for computational modeling, facilitating the simulation of intricate PDRC structures with relative ease. The modeling approach, exemplified in Chapter 3 through a detailed walkthrough with a busbar example, laid the foundation for all subsequent simulations.

This thesis has not only validated my COMSOL models against established theory but has also ventured into the modeling of Fresnel equations to observe the behavior of reflection coefficients across varying angles of incidence.

The core of our efforts was the computational modeling of PDRC designs from Hudgings Lab, layer by layer, revealing critical insights into their optical performance. Notably, the simulation results confirmed the imperative for PDRCs to exhibit high reflectivity within the solar spectrum, a requirement clearly illustrated by the limited reflectivity observed in the sole glass substrate model.

### 5.2 Future Directions

Moving forward, several avenues for further research can be identified:

1. Enhanced definition in the reflectance versus wavelength graphs for glass plus silver and glass plus silver plus PDMS models, possibly through the utilization of more detailed refractive index interpolation tables or functions.
2. Exploration of adding more materials on top of the PDMS layer to fulfill PDRC design criteria more effectively, experimenting with various thicknesses and refractive indices to exploit constructive interference across multiple interfaces more efficiently.
3. The translation of computational models into physical prototypes for empirical validation in lab settings, comparing simulated reflectance with real-world performance.
4. Development of reflectance versus angle of incidence models to aid in the characterization of PDRC behavior throughout the day, providing a benchmark for experimental testing on rooftop installations.

Building on these initiatives, we see a profound link between the principles of Distributed Bragg Reflectors (DBRs) and Passive Daytime Radiative Cooling Systems (PDRCs). PDRCs strive to facilitate cooling without the need for active energy input by effectively radiating heat into the expansive coldness of outer space. The spectral selectivity and reflective capabilities intrinsic to DBR structures could vastly improve PDRCs.

By emulating the multilayer approach integral to DBRs, PDRCs can fine-tune their design to reflect a substantial portion of the solar spectrum, thereby reducing heat gain, while promoting the emission of thermal infrared radiation to enhance cooling. This alignment of high solar reflectance and high thermal emittance is the cornerstone of PDRC technology, presenting a pathway to energy-efficient cooling solutions.

### 5.3 Final Remarks

This thesis not only validates the utility of PDRCs within the context of sustainable cooling technologies but also charts a course for their further development and application especially on the computational modeling front.

As we look to the future, the insights and methodologies presented here will serve as a valuable resource for those endeavoring to advance the efficiency and applicability of PDRCs and similar technologies in our collective pursuit of environmental sustainability and energy efficiency.

# Appendix A

## An appendix

### A.1 About Meshes in COMSOL Multiphysics

In the course of developing my thesis, particularly while working on the modeling of infrared light through a glass substrate using COMSOL Multiphysics™'s Wave Optics module, I encountered a significant challenge related to mesh generation. The initial attempt to create a mesh for the silica glass model, a slab with a radius of one meter and a thickness of 5 mm, resulted in an error message from COMSOL. The error indicated that the current physics settings necessitated a mesh comprising approximately 11 million elements, a requirement that raised concerns about potential out-of-memory errors or process locking. This requirement stemmed from the model's attempt to simulate the behavior of infrared light with a 1-micron wavelength within the specified computational volume.

The root cause of the issue was the physics-controlled meshing process attempting to generate a mesh that resolved details down to the wavelength of the light being modeled. Two potential solutions were proposed: significantly reducing the computational volume of the model or altering the computational method to one that did not necessitate resolution at the wavelength scale. Opting for the latter approach, I adjusted the computational method accordingly, which effectively addressed the meshing issue and allowed the project to proceed without the need for an excessively dense mesh.

When selecting a mesh size, it's crucial to take into account the scale at which your model operates. If your geometry is measured in meters but you're examining phenomena occurring at the nanometer wavelength scale, choosing an excessively fine mesh could lead to huge computational demands, including significant memory usage. This approach balances the need for detail with practical considerations of computing resources.

## A.2 Additional Resources and Materials Pertaining to This Thesis

You can find a more comprehensive ordered list of my thesis materials, including the COM-SOL mph files, in this GitHub repository.

# Bibliography

- [1] A. P. Raman, M. A. Anoma, L. Zhu, E. Rephaeli, and S. Fan, **515**, 540 (????), ISSN 0028-0836, 1476-4687, URL <https://www.nature.com/articles/nature13883>.
- [2] F. L. Pedrotti, L. M. Pedrotti, and L. S. Pedrotti, *Introduction to optics* (Pearson/Prentice Hall, ????), 3rd ed., ISBN 978-0-13-149933-1.
- [3] C. Multiphysics ®, *The modeling workflow in COMSOL®*, URL <https://www.comsol.com/video-training/getting-started/setting-up-and-running-a-simulation-with-comsol-multiphysics>.
- [4] M. Chen, D. Pang, X. Chen, H. Yan, and Y. Yang, **4**, e12153 (????), ISSN 2567-3173, 2567-3173, URL <https://onlinelibrary.wiley.com/doi/10.1002/eom2.12153>.
- [5] I. E. Agency, *The future of cooling: Opportunities for energy-efficient air conditioning*, URL <https://www.iea.org/reports/the-future-of-cooling>.
- [6] Y. Yang and Y. Zhang, **7**, 18 (????), ISSN 2329-2229, 2329-2237, URL <http://link.springer.com/10.1557/mre.2020.18>.
- [7] F. Trombe, **XV** (????), URL <https://unesdoc.unesco.org/ark:/48223/pf0000012927>.
- [8] R. Fortin, J. Mandal, A. P. Raman, and S. Craig, **4**, 101570 (????), ISSN 26663864, URL <https://linkinghub.elsevier.com/retrieve/pii/S2666386423003788>.
- [9] J. P. Bijarniya, J. Sarkar, and P. Maiti, **133**, 110263 (????), ISSN 13640321, URL <https://linkinghub.elsevier.com/retrieve/pii/S1364032120305529>.
- [10] M. M. Hossain and M. Gu, **3**, 1500360 (????), ISSN 2198-3844, 2198-3844, URL <https://onlinelibrary.wiley.com/doi/10.1002/advs.201500360>.
- [11] C. Multiphysics ®, application ID: 19275, URL <https://www.comsol.com/model/distributed-bragg-reflector-19275>.